AD-A096 626 TEXAS UNIV AT AUSTIN F/6 11/4
INTERFACE CHARACTER OF ALUMINUM-GRAPHITE METAL MATRIX COMPOSITE--ETC(U)
DEC 80 H L MARCUS N00014-78-C-0094
UNCLASSIFIED NL

1 OF 1
AD A096626

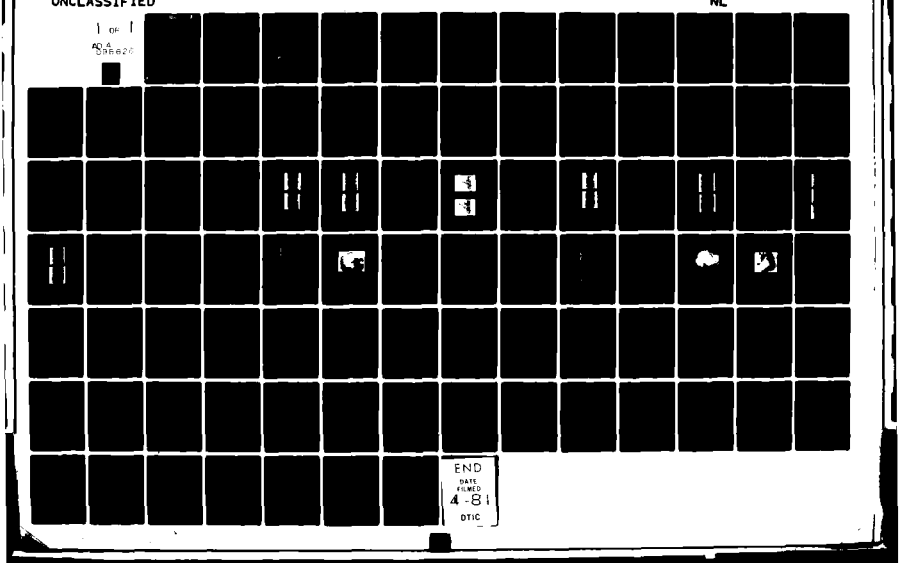

END
DATE FILMED
4-81
DTIC

LEVEL II

13

SECURITY CLASSIFICATION OF THIS PAGE (When Data Entered)

REPORT DOCUMENTATION PAGE

READ INSTRUCTIONS BEFORE COMPLETING FORM

1. REPORT NUMBER	2. GOVT ACCESSION NO.	3. RECIPIENT'S CATALOG NUMBER
	AD-A096 626	

4. TITLE (and Subtitle)
Interface Character of Aluminum-Graphite Metal Matrix Composites

5. TYPE OF REPORT & PERIOD COVERED
Dec 1 1979 - Nov 30 1980

6. PERFORMING ORG. REPORT NUMBER

7. AUTHOR(s)
H.L. Marcus (10)
Harris L. Marcus

8. CONTRACT OR GRANT NUMBER(s)
N 00014-78-C-0094

9. PERFORMING ORGANIZATION NAME AND ADDRESS
The University of Texas
Mechanical Engineering/Materials Science
TAY 167, Austin, TX 78712

10. PROGRAM ELEMENT, PROJECT, TASK AREA & WORK UNIT NUMBERS
(11) 23 Nov 80

11. CONTROLLING OFFICE NAME AND ADDRESS
Office of Naval Research
Metallurgy and Ceramics Program
Arlington, VA 22217
(12) 87

12. REPORT DATE
December 23, 1980

13. NUMBER OF PAGES
84

14. MONITORING AGENCY NAME & ADDRESS (if different from Controlling Office)
Dr. B.A. MacDonald, Metallurgy Division
Office of Naval Research, Code 471
Department of the Navy
Arlington, VA 22217

15. SECURITY CLASS. (of this report)
Unclassified

15a. DECLASSIFICATION DOWNGRADING SCHEDULE

16. DISTRIBUTION STATEMENT (of this Report)

DISTRIBUTION STATEMENT A
Approved for public release;
Distribution Unlimited

DTIC
ELECTE
MAR 27 1981
E

17. DISTRIBUTION STATEMENT (of the abstract entered in Block 20, if different from Report)

Approved for public release; Distribution unlimited.
9 Annual progress rept.

18. SUPPLEMENTARY NOTES
LIC-77-30 Nov 80.

19. KEY WORDS (Continue on reverse side if necessary and identify by block number)

Metal Matrix Composites, Al/gr composites, Auger Electron Spectroscopy, Residual Stresses, Interface Characteristics, Electron Loss Spectroscopy, Transverse Strength, Transmission Electron Spectroscopy, C Diffusion, Scanning Auger Microscopy.

20. ABSTRACT (Continue on reverse side if necessary and identify by block number)

The results of the research described in this annual report can be summarized in terms of the experimental approaches used. The TEM studies of the phases in the aluminum-graphite interface demonstrated their complex nature. The method of preparing the thin foils, either chemical etching or chemical polishing, influenced which of the phases were observed. The interface phases observed were oxides, carbides and borides. In the studies of the aluminum deposited on single crystals of graphite the interface oxide formed is a simple aluminum oxide. The thickness of the aluminum oxide layer →

DD FORM 1 JAN 73 1473 EDITION OF 1 NOV 65 IS OBSOLETE

SECURITY CLASSIFICATION OF THIS PAGE (When Data Entered)

347800

81 3 11 043

AD A096626

DTIC FILE COPY

in the interface of aluminum-graphite junction system appeared to control the switching phenomenon observed in I-V measurements. Two different stable conducting states are present in the memory switching effects after the functions were properly electroformed. These states were dependent on the oxide thickness at the interface. SAM analysis of the fractured junction areas indicate the interface seems to be more cohesive resulting in fracture within the graphite when the thinner oxide layer is present. However, when the thickness of oxide is beyond certain limits (~10 nm), the fracture occurs in the oxide/graphite interface region.

Initial SAM studies on the formation of Al_4C_3 indicate that the C from the graphite diffuses through the oxide and forms next to the aluminum matrix. In general the onset of Al_4C_3 occurs with a drop in longitudinal strength. The increase noted in transverse strength occurs after the decrease in longitudinal strength.

X-ray diffraction residual stress measurements show large residual stresses in the aluminum matrix both in the longitudinal and transverse directions. No correlation with the transverse strength of the composites was observed. Cooling the composites to liquid nitrogen temperature and reheating to room temperature reduced the residual stresses by approximately 30%, but had no significant influence on the transverse strength.

The pitch fiber composites had a lower residual stress than the expected value. This can be explained by either lack of constraint in the thin plates tested or poor adhesion in the interface.

Problems are described in doing detailed AES peak shift and shape analysis. For the carbon peak both the electron and ion beams damage the material resulting in a standard spectrum independent of the fiber measured. The SAM analysis combined with sputtering showed the oxide, boride, and carbide layer positions relative to the graphite to be very reproducible.

in the interface of aluminum-graphite junction system appeared to control the switching phenomenon observed in I-V measurements. Two different stable conducting states are present in the memory switching effects after the functions were properly electroformed. These states were dependent on the oxide thickness at the interface. SAM analysis of the fractured junction areas indicate the interface seems to be more cohesive resulting in fracture within the graphite when the thinner oxide layer is present. However, when the thickness of oxide is beyond certain limits (~10 nm), the fracture occurs in the oxide/graphite interface region.

Initial SAM studies on the formation of Al_4C_3 indicate that the C from the graphite diffuses through the oxide and forms next to the aluminum matrix. In general the onset of Al_4C_3 occurs with a drop in longitudinal strength. The increase noted in transverse strength occurs after the decrease in longitudinal strength.

X-ray diffraction residual stress measurements show large residual stresses in the aluminum matrix both in the longitudinal and transverse directions. No correlation with the transverse strength of the composites was observed. Cooling the composites to liquid nitrogen temperature and reheating to room temperature reduced the residual stresses by approximately 30%, but had no significant influence on the transverse strength.

The pitch fiber composites had a lower residual stress than the expected value. This can be explained by either lack of constraint in the thin plates tested or poor adhesion in the interface.

Problems are described in doing detailed AES peak shift and shape analysis. For the carbon peak both the electron and ion beams damage the material resulting in a standard spectrum independent of the fiber measured. The SAM analysis combined with sputtering showed the oxide, boride, and carbide layer positions relative to the graphite to be very reproducible.

Interface Character of Aluminum-Graphite Metal Matrix Composites

Annual Technical Report
Office of Naval Research
Contract N00014-78-C-0094

The University of Texas
Austin, Texas 78712

Principal Investigator
Harris L. Marcus
Mechanical Engineering/
Materials Science and Engineering

December 23, 1980

INDEX

Abstract

Interface Character of Aluminum-Graphite Metal Matrix Composites

The results of the research described in this annual report can be summarized in terms of the experimental approaches used. The TEM studies of the phases in the aluminum-graphite interface demonstrated their complex nature. The method of preparing the thin foils, either chemical etching or chemical polishing, influenced which of the phases were observed. The interface phases observed were oxides, carbides and borides. In the studies of the aluminum deposited on single crystals of graphite the interface oxide formed is a simple aluminum oxide. The thickness of the aluminum oxide layer in the interface of aluminum-graphite junction system appeared to control the switching phenomenon observed in I-V measurements. Two diff ·nt stable conducting states are present in the memory switching effects after the functions were properly electroformed. These states were dependent on the oxide thickness at the interface. SAM analysis of the fractured junction areas indicate the interface seems to be more cohesive resulting in fracture within the graphite when the thinner oxide layer is present. However, when the thickness of oxide is beyond certain limits (~10 nm), the fracture occurs in the oxide/graphite interface region.

Initial SAM studies on the formation of Al_4C_3 indicate that the C from the graphite diffuses through the oxide and forms next to the aluminum matrix. In general the onset of Al_4C_3 occurs with a drop in longitudinal strength. The increase noted in transverse strength occurs after the decrease in longitudinal strength.

X-ray diffraction residual stress measurements show large residual stresses in the aluminum matrix both in the longitudinal and transverse directions. No correlation with the transverse strength of the composites was observed. Cooling the composites to liquid nitrogen temperature and reheating to room temperature reduced the residual stresses by approximately 30%, but had no significant influence on the transverse strength.

The pitch fiber composites had a lower residual stress than the expected value. This can be explained by either lack of constraint in the thin plates tested or poor adhesion in the interface.

Problems are described in doing detailed AES peak shift and shape analysis. For the carbon peak both the electron and ion beams damage the material resulting in a standard spectrum independent of the fiber measured. The SAM analysis combined with sputtering showed the oxide, boride, and carbide layer positions relative to the graphite to be very reproducible.

I. Introduction

The aluminum graphite program has as a primary purpose determining the limiting factors that may control the transverse strength of the metal matrix composites. The focus of the research is in understanding how the graphite-aluminum interface influences the transverse strength. This report is an extension of the 1979 report [1] in which most of the initial data on the various approaches to evaluate the interface were described. The emphasis in this report will be on the recent advances in our research and how they relate to the prior work. The results reported here are from the experiments performed by Swe-Den Tsai, Duane Finello, James Lo and Dr. Michael Schmerling.

II. Experimental Approaches and Results

To probe the aluminum-graphite interface behavior a five pronged approach is being used. These include the following: 1. Determining the I/V characteristics of the interface between a single crystal of graphite and vapor deposited aluminum and comparing it with the failure mode of the interface as established by a peeling test. 2. X-ray evaluation of the differential thermal coefficient of expansion induced residual stress in the aluminum matrix. 3. Scanning Auger electron spectroscopy (SAM) analysis of the fractured interface determining the interface chemistry, chemical profiles in the vicinity of the interface chemistry, chemical profiles in the vicinity of the interface and evaluating chemical shifts in the AES spectra in terms of the chemical state at the interface. 4. Transmission electron microscopy (TEM) measurement

of the phases present in the interface. 5. The determination of the transport behavior for samples thermally treated to form aluminum carbide.

A list of materials tested is given in Table 1. In addition samples were made by ion sputtering aluminum on (0001) graphite single crystals. The single crystals were natural crystals obtained from Ticonderoga marble.

A. Current-Voltage (I-V) and AES Characterization of the Interface in the Single Crystal Graphite-Aluminum Junction System.

Natural graphite crystals dissolved from Ticonderoga marble were selected to obtain single crystalline material. The graphite crystals were extracted by leaching the mineral in concentrated HCl. The graphite crystals obtained are in disc or flake shape with a (0001) parallel to the surface as confirmed with TEM. The crystal surfaces were prepared virtually oxide free before ion sputtering deposition of commercially pure aluminum on them.

In order to monitor different aluminum oxide layer thicknesses sandwiched between the aluminum and graphite, the aluminum deposits were produced under various pressures in the deposition chamber. The deposits resulted in oxide thicknesses at the aluminum-graphite interface ranging from 2-20 nm angstroms. The details of the experimental preparation for the I-V samples and the associated peel tests as well as the detailed results are given in Appendix A. Only the highlights will be discussed here.

Table 1

Fiber Base	Matrix	Precursor Wire	Plate
Rayon	Al 201		G3394
PAN II	Al 201		G3437
"	Al 6061	T114A	G3675
"	"	T117	
**Pitch (VSB-32)	Al 6061	T105A	G3636
"	"	T133	G3842
"	"	T109B	
"	"		G4358
"	"		G4371
"	"		G4411
PAN II		Single Fiber Wire*	

*This composite wire was conducted by Toho Beslon Co. in Japan and produced by Celanese Corp. in the U.S.

**VSB-32 Pitch and P-55 Pitch Fibers are identical.

The tests can be classified into three groups. The first had a thin oxide layer at the aluminum graphite interface of about 2.0-4.0 nm. In this case the I-V curves were characterized by a high conductance state. The SAM measurements after the peel test showed the fracture path to be within the graphite substrate for the thin oxide. Group two contained samples with an oxide thickness of about 8.0 nm. The I-V characteristics showed a requirement for an electroforming process to get a conductance state. Subsequently the sample showed a switching phenomena from high to low conducting state with a stable high conducting state. The SAM peel test results were similar to that observed in the thin oxide material. The third group of samples had an oxide interface thickness of about 16.0-20.0 nm. These specimens could be put into an unstable high conductance state, which would decay back to the low conductance upon removal of applied voltage. The SAM peel test results showed that the fracture path was significantly within the interface oxide. These results imply that a thinner oxide interface, 3-10 nm is stronger than the thicker oxide interface, 15-20 nm, since the fracture path transferred from within the graphite basal planes to within the oxide itself.

The correlation of the change in fracture mode with the change in the switching characteristics of the I-V curves indicates the electronic state at the interface may play a major role.

B. Residual Stress Measurements Using X-Ray Diffraction Technique.

In this section measurements of the residual stress in the aluminum matrix phase developed due to the large difference in coefficient of thermal expansion between the graphite and the aluminum will be described. The details are given in Appendix B.

The high angle peak of aluminum (420) diffraction was used for the stress measurements to achieve high accuracy. The residual stresses were determined using both the ω-diffractometer system and the ψ-diffractometer arrangement.

The longitudinal direction residual stress values for Rayon/201 G3394 and PAN II/201 G3437 are comparable to the nominal 240 Mpa yield strength of the 201 Aluminum matrix. Relative low stresses also were measured in the VSB-32 pitch/6061 aluminum composites, G4371 and G4411. Because of the high modulus and thus the highly preferred orientation of basal plane along the fiber axis, a low axial thermal expansion coefficient is expected. Correspondingly, a large expansion mismatch should exist in the longitudinal direction of the fiber. The lower residual stresses observed could be attributed to the relaxation effect of the thinner composite plate used which contained two or three plies of precursor wires compared to the four to six layers with aluminum wrapping for the other plates. The average stresses in the aluminum matrix may not be fully constrained in the composite plates. Alternatively the bond strength may have been weak enough to fail during cooling, limiting the residual stress buildup. Further work is needed with the pitch base fibers.

When the high residual stress samples Rayon/201 G3394 and PAN II/201 G3437 composites were quenched in liquid nitrogen and annealed at room temperature, approximately 30% reduction in residual stress was observed. The cryogenic cooling induces additional plastic flow in the matrix, establishing a new elastic condition at the cryogenic temperature. Heating the composite back to room temperature will then relieve much of the residual stresses.

Thus, x-ray diffraction was applied to determine average residual stresses due to the mismatch in thermal expansion coefficients in the graphite-aluminum composite system. The results obtained indicate that the residual stresses averaged through the distribution in aluminum matrix are not directly related to the transverse strengths. The basic properties of the aluminum graphite interface region that are related to the transverse strength are the multiple interfaces between the various oxide, carbide and boride phases present in the gross interface. This complex interface structure also acts as a grated seal locally modifying the differences in coefficient of thermal expansion and the resulting residual stress pattern.

C. Scanning Auger Electron Spectroscopy of Aluminum Graphite Composites

The efforts in the SAM analysis of the composites continues to demonstrate the presence of an oxide at the graphite side of the interface. The structure of the oxide will be discussed in the TEM section. On the aluminum matrix side of the oxide is a titanium-boron rich region for materials prepared by the chemical vapor deposition process. The

modification of the interface chemistry by thermal treatment will be discussed in the section on aluminum carbide formation. The fracture surface chemistries associated with the peel tests were discussed previously.

One of the major attempts in this research program was to use peak shift changes as characterized by the deconvoluted spectra to relate to the local bonding. The use of the Auger peaks to define oxides, carbides, etc. continues to be very valuable to identify the gross phases in the interface region. The more subtle approach at separating out the matrix influence on the escaping Auger electron, such as plasmon excitation related peaks, from actual Auger peak shifts characteristic of the energy levels within the atom and relative intensities by the deconvolution approach has had a great deal less success. The problems were threefold. When studying the fiber surfaces, the electron beam used to excite the Auger electrons interacts with the graphite to drive the Auger spectra of all fibers to the same state as observed for pyrolytic carbon after it reaches a steady state condition with the incident electron beam. This spectra is very similar to that observed for normal contaminants on the surface. Under the inert argon ion beam the Auger spectra is also modified to contain the argon spectra and a different but fiber independent carbon Auger spectra. The spectra is different from that observed for the electron beam alone, but again only represents a beam modified spectra as opposed to a spectra representative of the original interface or fiber surface. Recent ESCA research [2] on pitch, rayon and PAN type fibers show peak shapes characteristic of carbonyl,

and lactone surface groups. These oxygen bearing radicals are weakly bound so that the Auger electron beam technique desorbs the material resulting in a much smaller apparent oxide concentration at the surface. The x-ray excitation used in ESCA does much less damage to the surface and with its better energy resolution, does a more complete characterization of the bonding. The possibility of using ESCA to study the fracture interface has been examined but the lack of appropriate special resolution greatly limits its applicability.

A third problem was the very slow convergence of the Fourier series used in the deconvolution techniques. This led to a decrease in the signal to noise content of the spectra. This problem is solvable by additional program modification, but combining the electron and ion beam modification to the measured Auger spectra and the program problems has led to the conclusion to greatly reduce the effort on this approach to gaining an insight into the interface.

D. Transmission Electron Microscopy of Phases Present at Aluminum Graphite Interface.

To determine the crystal structure of the phases present at the aluminum-graphite interface, TEM was performed on samples prepared using chemical thinning and electrochemical thinning techniques. The chemical solutions were concentrated HCl (12 M), HCl diluted with either 20% or 60-70% V% Methanol or 7N KOH solution. The electropolishing was carried out in a solution of 10 parts ethanol, 6 parts ethelene glycol and 1 part perchloric acid.

The results of the chemical thinning approaches were the determination of γ-Al_2O_3, TiB_2, and $Ti_{1-x}Al_xB_2$. The electrolytic thinning for the Al 6061/Pitch VSB-32 composites showed the presence of γ-Al_2O_3, $Ti_{(1-x)}Al_xB_2$, TiB_2, $MgAl_2O_4$ spinell, Mn_2TiO_4 and Al_3C_4. The different phase identifications demonstrates that the thinning technique will strongly influence which of the interface phases will remain. The combination of results obtained with both thinning techniques further demonstrates the extreme complexity of the aluminum graphite interface in the commercial materials. In the single crystal studies the interface oxide is aluminum oxide.

E. Aluminum Carbide Formation

One of the products of the thermal exposure of the composite during infiltration, consolidation and subsequent heat treatment is the Al_4C_3. The presence of large amounts of Al_4C_3 increases the transverse strength of the composite, but with simultaneous decrease in longitudinal strength. In addition the water soluble Al_4C_3 would make the interface extremely susceptable to environmental attack. For these reasons a series of studies were initiated to follow the kinetics of Al_4C_3 formation. The aim of the study was to see how the transport occurred, the kinetics of the transport and the possibility of thermal treatment resulting in enhanced transverse strength prior to the degradation of the longitudinal properties.

The first result was that there was very little evidence supporting the possibility of enhanced transverse strength before longitudinal

strength was degraded. In the pitch fiber -6061 Al alloy systems, the longitudinal strength was reduced before any signs of improved transverse strength. In the rayon base fibers a small increase was noted in transverse strength but the strength did not exceed two ksi before degradation of the longitudinal strength. In general this approach to improving transverse strength does not seem promising as seen from the experimental results as well as the intrinsic environmental sensitivity problem of the Al_4C_3.

The Al_4C_3 in the heat treated commercial aluminum graphite composites was found to form on the matrix side of the interface. This implies that carbon is diffusing through the oxide at the interface. The $Ti_{(1-x)}Al_xB_2$ phase seems to go into solution in the aluminum phase. The SAM results show there is a mixture of Al_4C_3 and $Ti_{(1-x)}Al_xB_2$ between the oxide and matrix after 520°C for 240 hours or 550°C for 24 hours. After 240 hours at 550°C the Ti and B signals are very diffuse and a very thick Al_4C_3 exists.

To get a more detailed measure of the Al_4C_3 formation a series of measurements are underway on the single crystals described earlier. The growth rate as a function of oxide thickness and temperature will be determined.

III. Discussion and Conclusions

Through the thorough examination applying the various experimental approaches previously discussed, the presence of many phases were identified as the intermediate phases in the graphite-aluminum interface.

These multiple phases of different crystallographic structures and lattice parameters comprise an incoherent interface between the graphite fiber and aluminum matrix. The complex structures of the intermediate phases existing in the interface will have considerable effect on the interfacial energy, and thus on the cohesive strength as well. The appreciable residual stresses measured in the aluminum matrix indicate that mismatch in the thermal expansion coefficients serve to significantly alter the stress at interface. The existence of intermediate phases could possibly further change these stress patterns resulting in complicated stress gradients across the multiplephase-interface. This would be expected to influence the interface cohesion although no direct correlation was observed between the x-ray residual stress measurements and the transverse strength.

In the practical fabricating process of the aluminum-graphite composite materials, a large area of free graphite fiber surface is to be converted to the well-bonded, force-transmitting interfaces. The first requirement for the formation of a highly cohesive and stable interface is the good wetting of the graphite fiber by the matrix or by the intermediate layers between the matrix and fiber. During the formation of the interfaces the properties of the constituents including the pretreatment coating (like TiB_2) may be altered because of a variety of factors. These include preferential surface absorption, catalytic effects on the surface, chemical reaction or differential thermal effects. Therefore, new phases like aluminum oxide, aluminum carbide, etc., may be formed or the mechanical states of stress near the interface can be modified. For

this reason, the phases that exist in the interface region between aluminum and graphite fiber become the primary controlling factors for the interface strength.

The intermediate compound formed in the interface could be the product of the reaction between metal matrix elements and oxygen absorbed on or contained within the fiber surface as well as the pre-coating layers. An example is the aluminum oxide formed adjacent to the surface of graphite fiber. For example the γ-Al_2O_3 identified in this study is a low temperature structure of the Al_2O_3. It has been reported recently [3] that surface treatments of graphite fibers which promote better fiber--epoxy matrix adhesion result in an increase in surface oxygen concentration as measured by XPS and an increase in total surface free energy of the graphite fiber surface. This effectively increases the work of adhesion resulting in the improvement of the interface bonding. The change in the surface energy comes about primarily from an increase in the polar component of surface energy by increasing surface polarity as well as the surface concentration of oxygen. It has also been pointed out [4] that nitric acid oxidation of a PAN type fiber prior to incorporation into epoxy resin matrix increases the bonding strength between fiber and matrix. This suggested that these surface oxide or surface groups were important in enhancing the interface bonding. Thus, in an analogous manner oxygen or oxide on the fiber surface seems to promote the wetting by aluminum. The formation of this stable oxide layer appeared to improve the transverse strength.

The existence of the precoated TiB_2 or $Ti_{(1-x)}A_xB_2$ layer on the graphite fiber surface, however, could affect the kinetics of the

interface reaction for the aluminum oxide. The roles of the boride phase may be as diffusion barrier, or having a catalytic effect involving the active sites for oxide formation involving the surface crystallography and the presence of defects and ripple features observed with TEM. When the boride layer, graphite substrate and aluminum matrix are subject to the differential thermal stresses, the reaction mechanism might be further modified by the induced microstrains. The nature of the bonding or the interaction between phases in the interface also affects interface cohesion. The bonding between aluminum graphite and graphite is interlocking through the porous sites on the fiber surface. It is particularly obvious after the graphite fibers are heavily degraded by the formation of carbide.[5] The formation of the surface oxide, however, is not detrimental to the fibers and the nature of the bonding between aluminum oxide and fiber is apparently of chemical origin. A possible speculation is that the oxide phase might interact with fiber surface through the Van der Waals force or induced dipole interaction. This secondary bonding involves an interaction distance 3-5 Å. This leads to theoretic strengths on the order of 10^3 to 10^4 Mpa [6] assuming the atoms or molecules are at proper bonding distances. However, in most of the cases the ideal condition of perfect molecular contact is not leading to the primary loss of interface strengths.

The aluminum oxide probably is not the unique strengthening species. The parameter which is most likely to be of significance in this respect is the average number of bonds formed between the matrix and graphite surface per unit length of fiber. The interphases must be physically

stable and easily achieve intimate bonding distances with the graphite surface. Aluminum oxide is a convenient one, since aluminum easily forms a thin layer of oxide. When the oxide grows in the thickness dimension, the nature of this layer becomes more susceptible to fracture. The exact alteration of this nature is not clear but is possibly related to the formation of the microvoides or other defects leading to the heterogeneous nucleation of the cracks.

Even if good wetting is initially attained, the changing temperature following the infiltration in the fabrication procedures of composites would also tend to modify the interface cohesion. In particular, the residual stresses at the interfaces resulting from the differential shrinkage at phase boundaries could lead to undesirable stress concentrations. It was found in the residual stress measurements that the average residual stresses developed in the aluminum matrix do not directly correlate to the transverse strength of the composites. In the immediate vicinity of the boundaries between each interphases or aluminum and graphite, the local residual stresses and voids due to the difference in thermal expansion coefficients could still be deleterious to the interfacial cohesion and overall transverse strength.

The electronic characterization studies reported here shed a light on the character of the aluminum-graphite interface problem. More specifically the oxide phase in the interface between the graphite and the aluminum was studied. The samples were made by choosing simple component materials and fabricated in a way under which the physical conditions are simplified. Because of the small areas of interface and more ideal experimental conditions involved, better control of the oxide

was attained. In particular the oxide thickness effect was observed. The application of controlled oxide thickness to the production of commercial quantities of composite materials will be difficult since the conditions which influence the interface bonding become far less controlled and more complicated than the ideal situation presented here.

IV. Summary

The results of the research described in this annual report can be summarized in terms of the experimental approaches used. The TEM studies of the phases in the aluminum-graphite interface demonstrated their complex nature. The method of preparing the thin foils, either chemical etching or chemical polishing, influenced which of the phases were observed. The interface phases observed were oxides, carbides and borides. In the studies of the aluminum deposited on single crystals of graphite the interface oxide formed is a simple aluminum oxide. The thickness of the aluminum oxide layer in the interface of aluminum-graphite junction system appeared to control the switching phenomenon observed in I-V measurements. Two different stable conducting states are present in the memory switching effects after the functions were properly electroformed. These states were dependent on the oxide thickness at the interface. SAM analysis of the fractured junction areas indicate the interface seems to be more cohesive resulting in fracture within the graphite when the thinner oxide layer is present. However, when the thickness of oxide is beyond certain limits (10 nm), the fracture occurs in the oxide/graphite interface region.

Initial SAM studies on the formation of Al_4C_3 indicate that the C from the graphite diffuses through the oxide and forms next to the aluminum matrix. In general the onset of Al_4C_3 occurs with a drop in longitudinal strength. The increase noted in transverse strength occurs after the decrease in longitudinal strength.

X-ray diffraction residual stress measurements show large residual stresses in the aluminum matrix both in the longitudinal and transverse directions. No correlation with the transverse strength of the composites was observed. Cooling the composites to liquid nitrogen temperature and reheating to room temperature reduced the residual stresses by approximately 30%, but had no significant influence on the transverse strength.

The pitch fiber composites had a lower residual stress than the expected value. This can be explained by either lack of constraint in the thin plates tested or poor adhesion in the interface.

Problems are described in doing detailed AES peak shift and shape analysis. For the carbon peak both the electron and ion beams damage the material resulting in a standard spectrum independent of the fiber measured. The SAM analysis combined with sputtering showed the oxide, boride, and carbide layer positions relative to the graphite to be very reproducible.

References

1. Marcus, H.L., Annual Technical Report ONR Contract N00014-78-C-0094 (December 1979).

2. Hopfgarten, F., Fiber Sci and Tech., 12, (1979) 283.

3. Hammer, G.E. and Drzal, L.T., Application of Surface Science 4, (1980) 340.

4. Herrick, J.W., 23rd Am. Tech. Conf., SPI Reinforced Plastics/ Composites Division, Sec. 16-A (February 1968).

5. Khan, I.H., Met. Trans. 7A (1976) 1281.

6. Mykura, H., Solid Surfaces and Interfaces, Dover Pub. (1966).

Appendix A

Current-Voltage (I-V) and AES Characterization of the Interface in the Single Crystal Graphite-Aluminum Junction System

In most of the experimental approaches used to characterize the interface in the anisotropic graphite aluminum composite system, the actual interface is destroyed for the test to be made. This is particularly true for the AES and TEM studies. In an attempt to evaluate the interface in a non-destructive manner the I-V characteristics of planar composites of aluminum on graphite with an oxide interface were studied. These results are then correlated with AES measurements on the peeled interface. The results presented here come from the dissertation of Swe-Den Tsai. The experimental approaches are presented first followed by the results and interpretation for both the I-V and AES measurements.

A. Preparation of Aluminum/Graphite Junctions

Natural graphite crystals dissolved from Ticonderoga marble were selected to obtain single crystalline material. They are the most convenient and highly perfect graphite crystals

known,[1] and the ones on which the widest range of fundamental experiments have been successfully carried out.[1] The chemistry of the marble is calcite base. The graphite crystals were extracted by leaching the mineral in concentrated HCl. The graphite crystals obtained are in disc or flake shape.

To assume that the surfaces are oxygen or oxide free before depositing aluminum on them two different cleaning procedures were followed:

(1) In the first approach, the graphite crystals were ultrasonical cleaned in methanol. After being washed in deonized water the graphite crystals were dipped into a hydrofluric acid (HF) solution made of equal parts of 48% HF and deionzed water. Then the materials were rinsed thoroughly in deionized water.

(2) In the second approach, the top few layers of graphite crystals were peeled by placing scotch tape on both sides of the disc and pulling the two pieces of tape apart. This exposed very clean internal surfaces of the crystal resulting in thinner crystals. The surface state or structure may have been altered during the pealing procedure.

Examination in the Auger spectrometer showed that both of the cleaning methods gave highly oxygen free surface. The surface occasionally contained very small amounts of oxygen, less than a monolayer, for the crystals cleaned by the HC procedure.

For the naturally formed disc or flake shape of graphite crystals, the basal planes are parallel to the surface of crystal

disc and the C axis direction is thus normal to the surface. This crystallographic orientation was verified by TEM electron diffraction patterns on thin graphite crystals obtained by repeated peeling. The hexagonal symmetry of single crystal diffraction patterns indicated that the zone axis (0001) is normal to the surface of the sample.

Aluminum-graphite junctions were prepared by deposition of commercially pure aluminum (about 0.9975 or aluminum) onto the surface of the peeled graphite crystals by vacuum evaporation. Proper masks were made to evaporate aluminum dots onto the graphite crystal with diameters of approximately 1 mm. One or two of these evaporated junctions were made on a graphite crystal substrate. To make sure the probe electrodes made good ohmic contacts, both gold and aluminum dots were deposited on the same substrate for the electrical testing. The geometry is shown schematically on Fig. A-1 (a).

In order to monitor different aluminum oxide layers sandwiched between aluminum and graphite, the aluminum deposits were produced under various pressures in the deposition chamber. These can be categorized as the following:

(1) The aluminum was deposited in a high vacuum at a pressure of 4.0×10^{-7} Torr. (high vacuum low oxygen deposition)

(2) The aluminum was deposited at a pressure of $1\sim2 \times 10^{-4}$ Torr. (medium vacuum medium oxygen deposition)

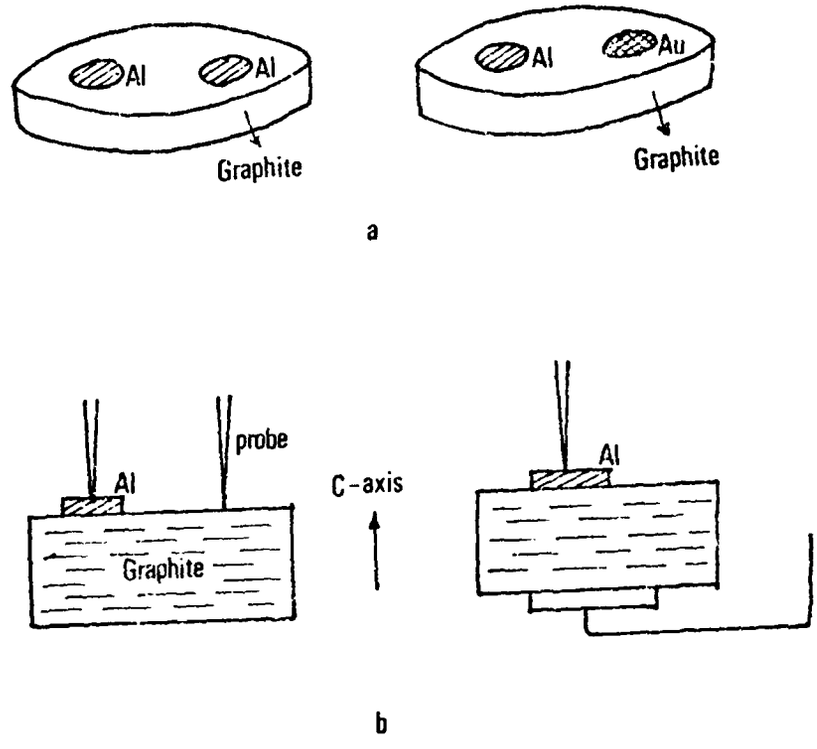

Fig. A-1 (a) Junction geometry of Al/Gr and Al/Gr+Au/Gr systems.
(b) Two types of contract configuration.

(3) The aluminum was slowly deposited at two stages of pressure. First, at $8x10^{-4}$~$2x10^{-3}$ Torr, then at $4x10^{-4}$ Torr. (low vacuum high oxygen deposition)

B. Measurement of Current-Voltage Characteristics

The current-Voltage (I-V) relationship of a junction system is of paramount importance in determining the electronic characteristics and internal physical effects. The I-V curve measurements were made with a curve tracer for various specimens. The electrical contacts used here were tungsten or osmium probes manipulated by a micropositioner system designed for standard I-C tests. A mercury drop was applied to the tips of probes to improve the mechanical stability. The I-V curve of contacts between mercury and graphite, and mercury with aluminum were tested first and proved to be ohmic and highly conducting. In order to examine two different current paths, two types of contact geometry were made:

(1) Planar contacts:

Both probes were contacted on the same crystal surface, one on the aluminum dot, the other on the graphite.

(2) Back contacts:

One probe was contacted on the aluminum dot, but the other electrode was bonded with conducting glue on the opposite surface of the crystal.

These two configurations are illustrated in Fig. A-1. In the specimens with planar contacts, the layer portion of current

passing through the basal plane of high conductivity makes the electronic transport different from the back contact specimens where the current is passing alone the low conductivity path normal to the (0001) plane.

C. Peeling Test and AES in Aluminum/Graphite Junction System

In addition to the I-V curve characterization the specimens produced under the various deposition vacuum pressures were also tested mechanically to determine the fracture behavior of the interface regions. A quick dry glue was applied at one end of a probe then fully aligned with the aid of a microscope to stick to the center area of the aluminum dots. After sufficient time, the probe was lifted and the center portion of aluminum dot was peeled away from the crystal.

The peeled areas of many of the two-aluminum dot specimens were thoroughly examined by SAM in the various specimens. The AES depth profiles were also taken by sputtering through the aluminum dots to investigate the thickness of the oxide formed at the aluminum/graphite interface.

A differential argon ion sputtering gun combined with AES was used to depth profile the aluminum dot. The ion sputtering rates were calibrated to be about 2.0nm per minute and 11.0nm per minute for aluminum oxide and aluminum metal respectively. The ion energy and ion current density used were 3KV and 140$\mu A/cm^2$ over a rastered 3x3 mm square region.

D. Results and Discussion of I-V Characterization

Generally, the current levels or conductance measured in planar contact specimens were approximately two to three orders higher than those in the back contact specimens. This large difference in electrical conductance could be attributed to the anisotropy of electrical conductivity in graphite crystal that was described in the introduction.

Some of I-V curves for planar contact samples are presented in Fig. A-2 and Fig. A-3. In Fig. A-2 the probes contacted the aluminum and graphite, but in Fig. A-3 the graphite side contact was made indirectly on a gold dot which was deposited by vacuum evaporation to improve the probe contact on the graphite. In both cases the I-V curves are linear below 0.1 volt bias. When higher voltages were applied, the curves deviated from linearity. When the voltages were still higher, the I-V characteristics were no longer symmetric and a weakly rectifying property occurred. The more conductive I-V character was found when the positive voltage was applied at the graphite contact. Since this also holds in most situations to be discussed, it is thus convenient to define the forward bias to be the polarity when positive voltage is applied to the graphite side, and the reverse bias when negative voltage is applied to the graphite side, unless otherwise noted. For better comparison at low currents and voltages, the zero points were shifted for the photographs. The right part and left part of the I-V curves are for forward and reverse bias respectively, as shown in Fig. A-2 (b) and Fig. A-3. This plotting technique is used for all the subsequent figures.

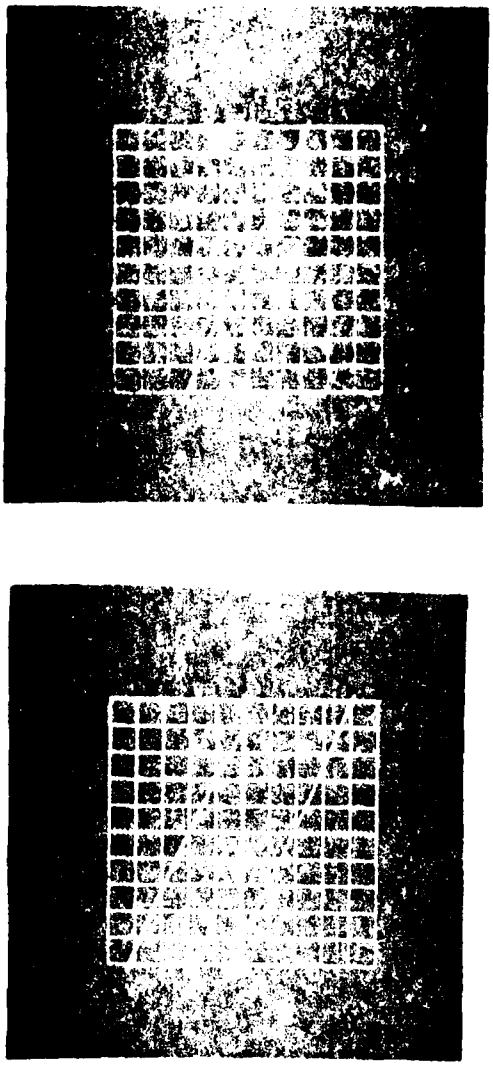

Fig. A-2. Example of I-V [illegible] contacts on aluminum and graphite.

Scale: Vertical [illegible] (b) 59 mA/div.

Horizontal [illegible] div. (b) 0.1 V/div.

In (b), right [illegible],

left [illegible].

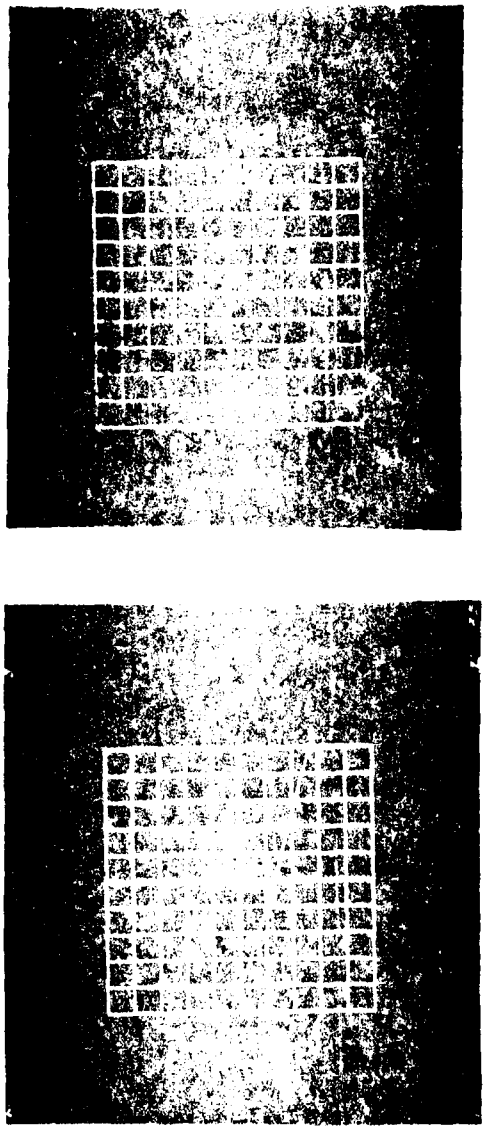

Fig. A-3. I-V curve t[illegible] aluminum and gold

Scale: Ver[illegible]

[illegible]

In (b), [illegible] to 0.8~0.9 V.

In addition to the weak rectifying behavior, a change in current-voltage dependence, a higher conductance state, arose after the voltage was increased to 0.8~0.9 volt (see Fig. A-3 (b)). This increase of conductance could be due to an electroforming process occurring at the junction regions. No obvious switching phenomena were observed. All the planar contact samples measured were prepared under the chamber pressures of $2\sim5\times10^{-5}$ Torr.

For the specimens of back contacts, the memory switching phenomena was found in most samples, which were sandwiched with adequate oxide layers between the aluminum and graphite. The I-V characteristics will be discussed according to the vacuum under which the samples were prepared and will be related to the oxide thickness (see the sample preparation section).

(1) High vacuum sample:

No electrical forming process was necessary to present a reasonable conducting state for the samples prepared under high vacuum circumstances. Either no switching was observed or a very weak switching from an unstable lower conductance state to a stable high conductance state was found when the sample was reverse biased. Occasionally, the very weak transition from high conductance state back to the low conductance state also happened in the forward bias, but this lower conductance state was not stable enough and eventually transferred to a stable high conduction state. The stable high conductance state described here is shown in Fig. A-4. The slope of

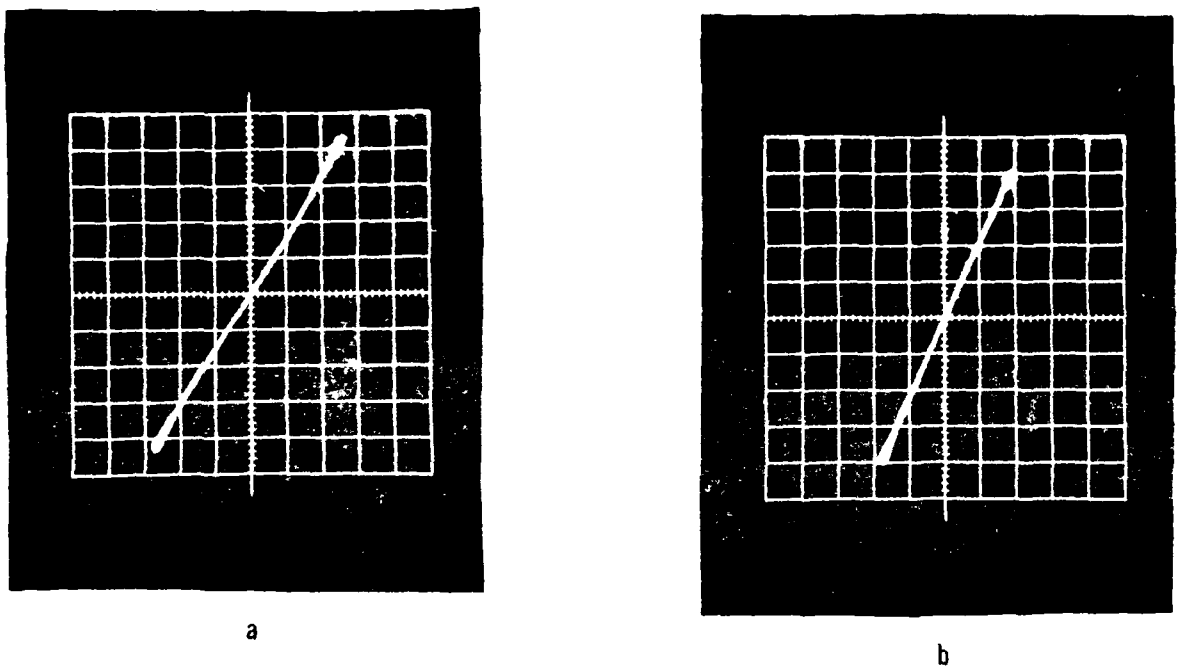

a b

Fig. A-4. I-V characteristics of samples prepared in high vacuum; for

(a) Peeled cleaning, I 5mA/div., V 0.1V/div.

(b) HF cleaning, I 10mA/div., V 0.1V/div.

low conductance state is approximately 1/2~1/3 of that of high conductance state.

(2) Medium vacuum samples:

The samples produced in this condition exhibited memory switching phenomenon, which were either irreversible or reversible for different conductance states. Here, most samples required a certain electroforming process to get increased conduction. One or two volts forming voltage with proper polarity was required. Once the samples were formed, threshold switching appeared.

The reversible switching I-V curves are given in Fig. A-5. After high field forward bias forming, the junction transit from a high resistance to a low resistance state with the I-V characteristics seen in Fig. A-5 (a). When the voltage is driven up to a threshhold value, Vth, (point B), here approximately -0.6~-0.9 V, the curve switches to a higher conductance state (line D)) as shown in the higher conducting part of Fig. A-5 (b). The conductance of this new state can be represented by the slope of CD. The ratio of high to low conductance is about 8 to 10.

Now, the polarity of the electric voltage is reversed, to the forward direction here, with the same voltage applied, the sample then still stays in the high conducting state (see forward bias part of I-V curve in Fig. A-5 (b)) represented by the slope of A'B'. When the current (or voltage) reaches a threshold current Ith at point B', here about 70~80 mA, the sample switches back to the low conductance

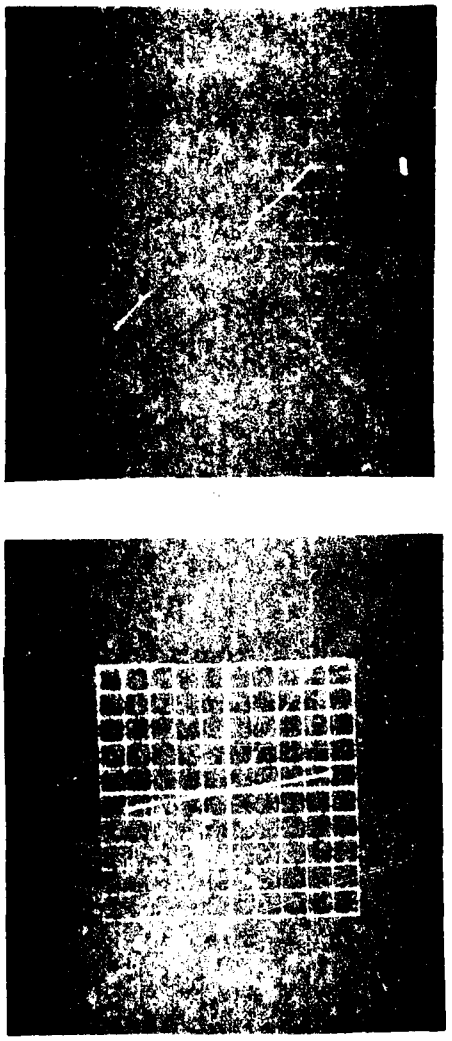

Fig. A-5. The I-V curve ... hing in medium vacuum sample

(a) conduct...

scale: ... /div

(b) switchin... ...h conducting states.

scale: ... v.

state (line C'D') as shown in lower conduction of the forward bias in Fig. A-5 (b).

It is noted that memory effects were also present in this type of sample. After switching, if the voltage is applied once more, the high or low conductance state is memorized by the sample. Actually four separated sections of I-V curve were used through the memory states of the sample for taking the photograph presented in Fig. A-5 (b). In the high conductance state the sample behaves almost like a ohmic resistor.

Instead of this reversible memory switching, most samples of the medium vacuum type demonstrated the irreversible memory switching effects. The high conductance states did not switch back to the low conductance state after the threshold switching from low to high conductant states. Only a tendency toward lower conductivity was observed when sufficiently high current (or voltage) was applied. Fig. A-6 shows an example of irreversible memory switching effect. Both the high and low conductance of each state vary a little from sample to sample. According to the memory switching observed in chalcogenide,[2] a semiconductor heterojunction or glass and amorphous[3] semiconductor, a current pulse must be used to trigger reversion of the memory material from the high conductance to the low conductance states for the irreversible switching situation.

(a) Low vacuum samples:

In low vacuum samples, an even higher electroforming field was required to induce a conducting state. Before forming, such

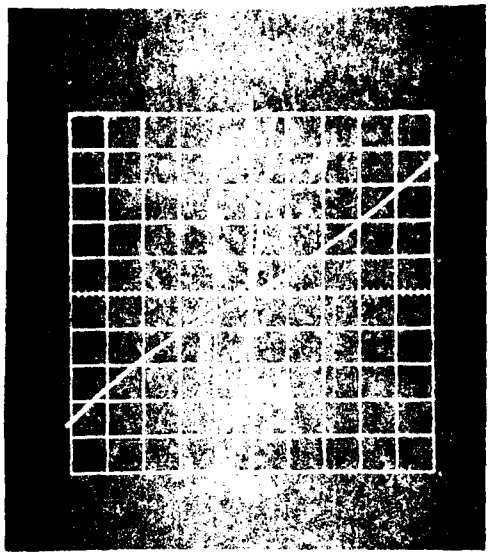

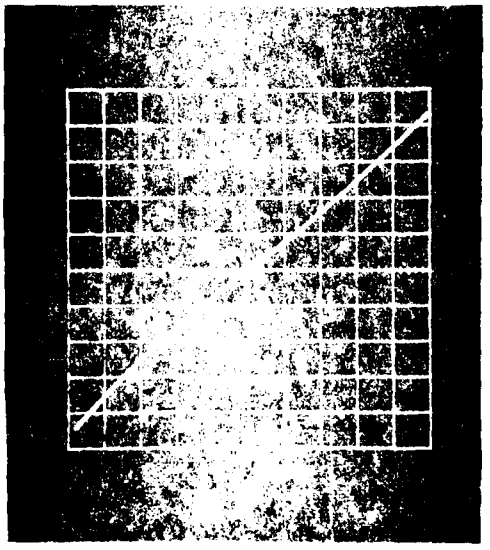

Fig. A-6. An I-V [illegible] switching
Scale: [illegible] div.
[illegible]
(b) is [illegible] ductance part of (a).

samples show a very high resistance and easily can stand a much higher voltage than in the normal state after forming. To form these samples, the voltage was increased slowly up to 10 V.

Two levels of switching effects were found here. In Fig. A-7 the low conductance state switched to a higher one (see Fig. A-7 (b)) after a threshold, Vth -1.2--1.4V, was reached. Then the bias was reversed the I-V curve shape changed gradually to the lower conductance states as shown in Fig. A-7 (c), and finally transferred to a low conductance state similar to its initial state (see Fig. A-7 (a)). Another higher level switching phenomenum occurred if a high field was quickly reversed to the sample. The higher conductance then obtained is shown in Fig. A-8 (a). This state switched to an even lower conductance state after the high voltage was again driven quickly in the forward biasing direction. This lower conduction state can be seen in Fig. A-8 (b), where different scales of current are used.

All the current-voltage relationships discussed for the back contact samples indicate that the degree of contamination in various vacuum conditions during the aluminum deposition strongly influences the electronic characteristics and also the interfacial chemistry. The use of different vacuum pressures during the aluminum depositions resulted in the thickness of aluminum oxides formed at interface between metallic aluminum and graphite crystal ranging from 3nm to 20 nm. Furthermore, through the AES studies on the peel fractured interfaces

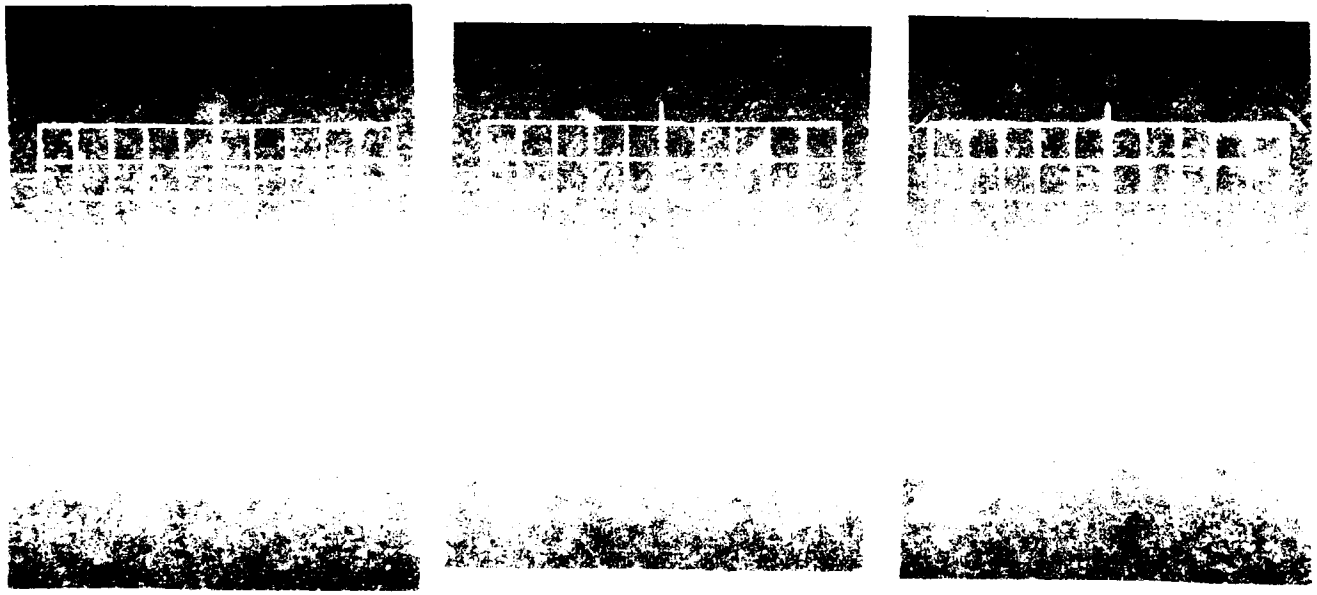

Fig. A-7. Low level switching effect.

(a) I: 0.2mA/div., V: 0.1V/div.

(b) and (c) I: 0.2 mA/div., V: 0.2V/div.

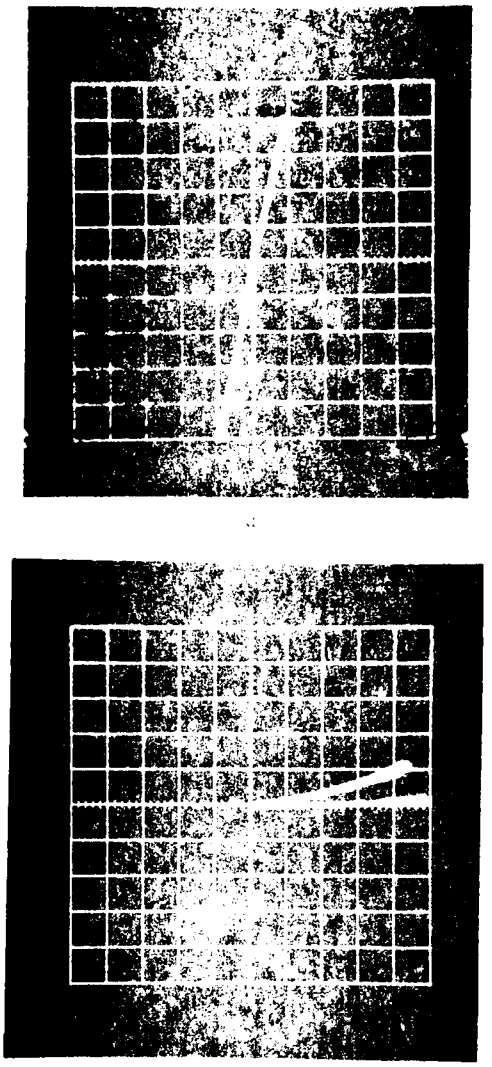

Fig. A-8. High level

(a) I: 5

(b) upper . lower: I: 0.2mA/div.

V: 0.2

produced in various vacuum conditions, the interfacial cohesive property will also be correlated to the oxide thickness.

In the case of high vacuum prepared samples, the AES determined 2nm thick oxide is so thin that the carriers could easily tunnel through and almost no blocking effect results at low electric field. The very weak switching or unstable low conductance state might be the result of not enough trapping states which depends on the nature of interface layer or the high current density dominating at the interface region.

When the oxide is thicker (about 8-16 nm as the situation in the samples prepared by medium and vacuum, the forming field required is on the order of 10^6 V/cm, which corresponds to the required high field for the electroforming process.[4] Actually, the fields at or near geometric irregularities of the oxide layer such as protrusion, could be considerably greater than in a plane parallel structure of the same average thickness. This implies that forming may be initiated by these local high fields.[5]

In the threshold switching phenomena, one could expect that a strong electric field could ionize both the traps and electrons from the valence band. The switch to high conduction occurs after attaining a field in which the electron carriers reach a certain level. After the high external field is reduced or switched off, the carriers are trapped and cannot recombine. In the next switch, the reversal of field yields a hole flow

toward the high field protrusion area, and when the field ionization probabilitity is high enough, the electrons recombine with holes and the conductance decreases.[6]

Another speculation[7] is that the threshold voltage might introduce a kind of micro-protrusion near the interface with oxide, possibly close to aluminum side where the irregularities filled with aluminum metal are originally the points of the highest intensity of the field. These newly formed protrusions are fluctuated in a higher root mean square value (rms) than the original interface. The reduction in local tunneling distance then creates a significant tunneling current through the interface. When the field is partially reversed, a restoring process starts to decrease the curvature of the protrusion and effectively decrease the rms value of the protrustion. The current then drops rapidly and switches back to the lower conductance state.

E. Results and Discussion of Peeling Test and AES Investigation

Peeling tests were made on samples corresponding to the three different vacuum conditions and electrical behaviors discussed in the last section. The specimens were loaded in ultra-high vacuum chamber of SAM as soon as the peelings were made. Results will be presented for the three types of samples.

(1) The fractured area of the peeled aluminum dot for samples produced under high vacuum exhibited the same surface chemistry as the oxygen free graphite surface cleaned by the

peeling process. An AES spectrum of this area is given in Fig. A-10. The SEM picture of the fracture surface is also given in Fig. A-11. This result here indicates that the interface is relatively stronger in cohesion than the bonding between layers of the graphite crystal, and therefore the fracture paths occur inside the graphite, mostly along the basal planes. The evidence of this type fracture behavior is also strengthened by the AES study on a peeled edge layer which is the image part of the peeled substrate. This graphite rich layer can also be seen in Fig. A-11. An AES depth profile monitoring aluminum, oxygen and carbon composition in the neighborhood of the interface is also shown in Fig. A-12. Based on the calibrated sputtering rate for aluminum oxide the thickness of the oxide on the interface is estimated to be about 3 nm. An approximately 4 nm thick layer of oxide also was observed in the other high vacuum sample.

(2) A similar surface chemistry has also been observed on the peeled area for the medium vacuum samples. The fractured surface is as clean as a freshly peeled graphite crystal. The oxide thickness at the interface is about 8 nm as is presented in Fig. A-13.

(3) In the low vacuum prepared samples, however, a careful examination of AES through the peeled fractured surface showed that most areas contain some amount of aluminum oxide which appeared to be gray in the SEM contract, and some darker areas were identified to be the clean oxygen free graphite

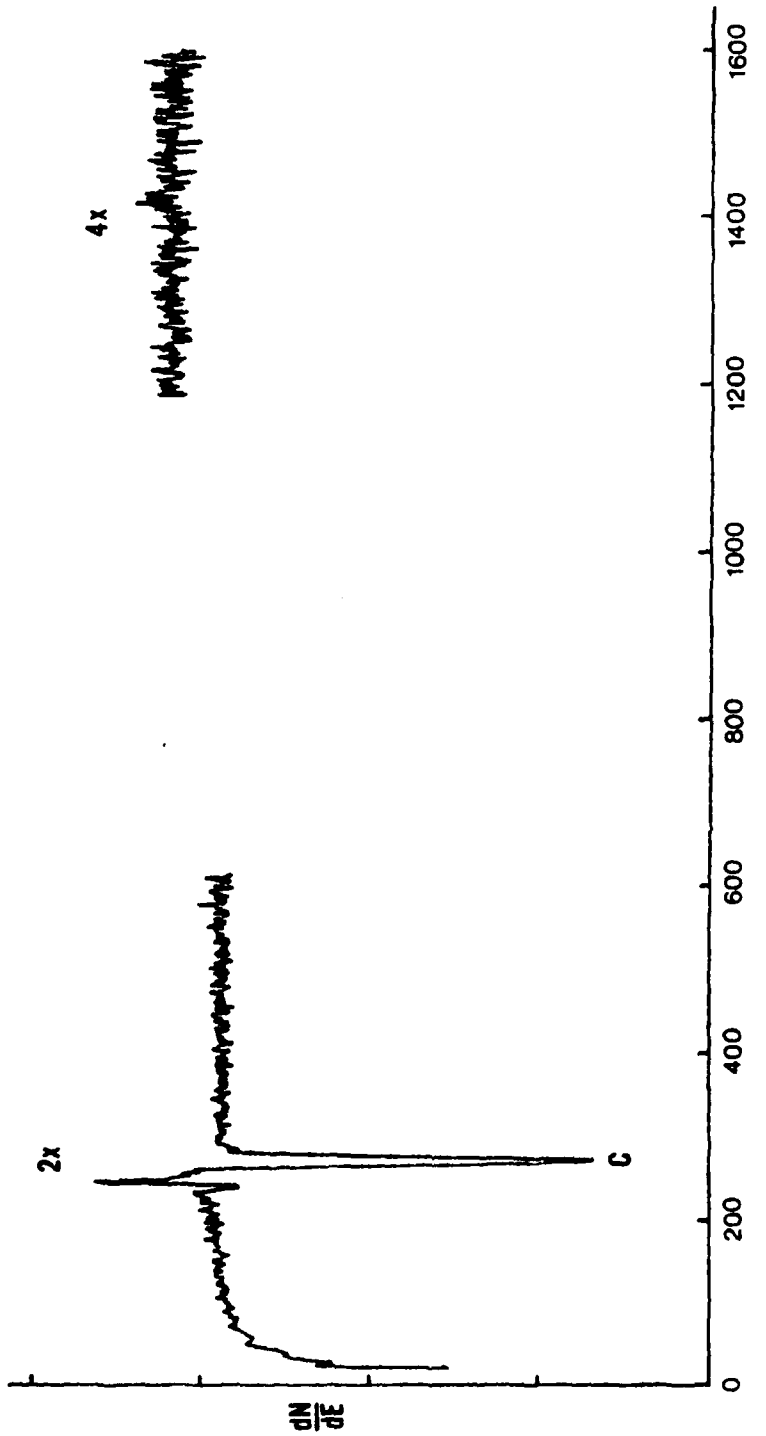

Fig. A-10. AES of peeled area in samples prepared in high vacuum.

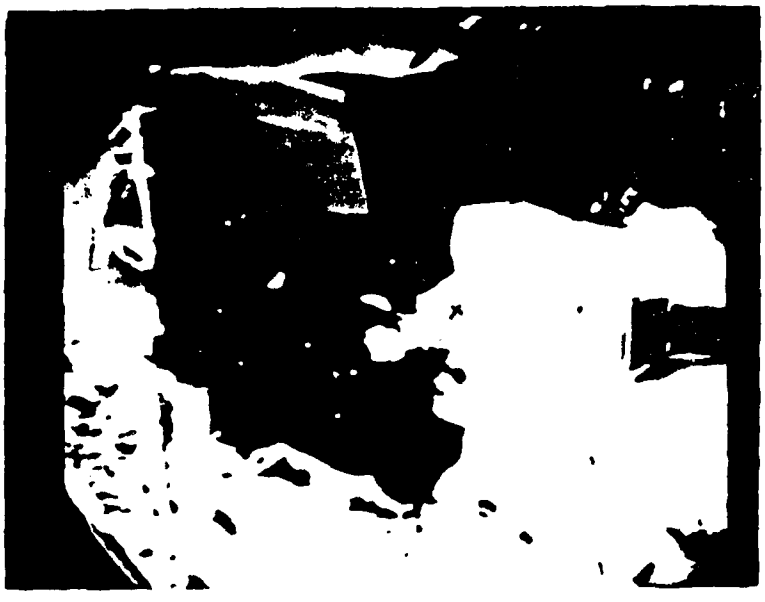

Fig. A-11. The SEM picture of peeled area for high vacuum sample.

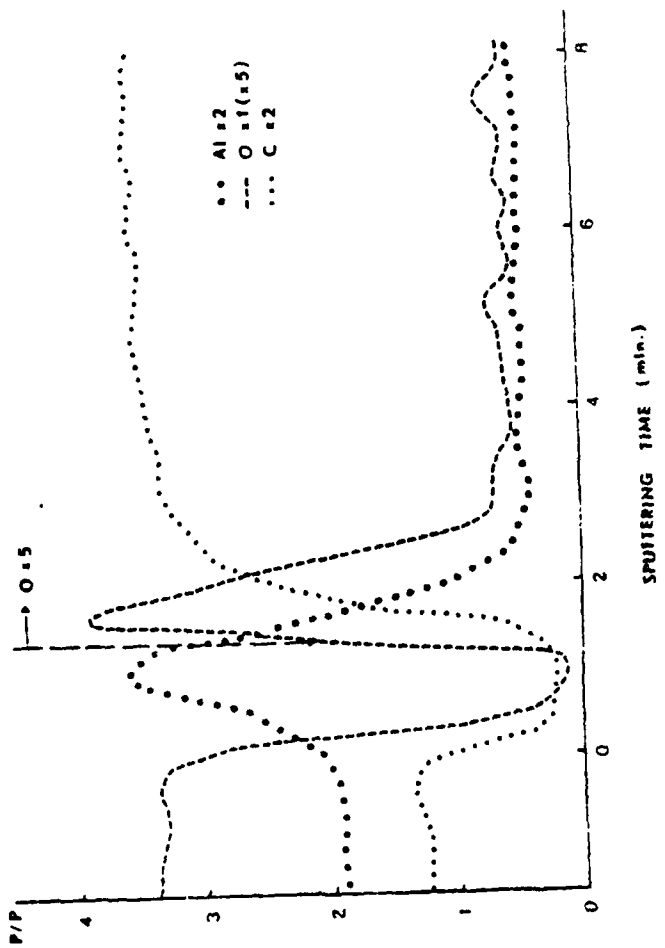

Fig. A-12. AES depth profile showing the interface chemistry of high vacuum sample.

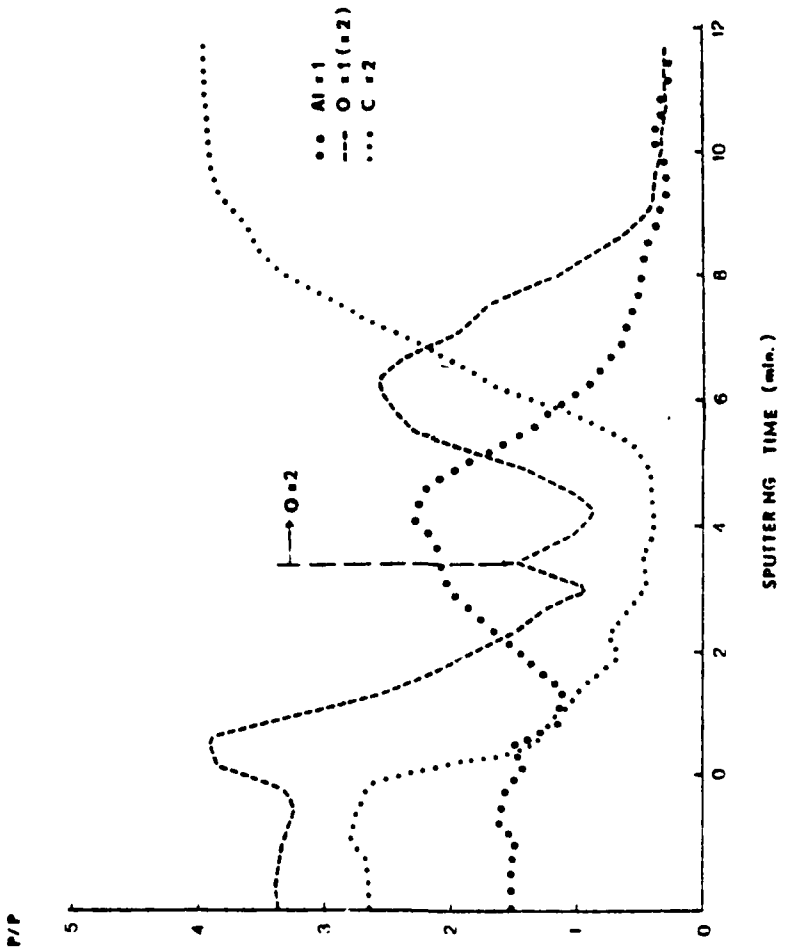

Fig. A-13. AES depth profile for medium vacuum samples.

surface. One of the AES spectra taken in oxide area on the graphite substrate is presented in Fig. A-14(a). The SEM fractograph showing rough and dimpled features is shown in Fig. A-15(a). A scrap as an image side of the peeled fractured surface exhibits appreciable oxide content which appears to be greater than that of substrate side. The AES spectrum and SEM picture are also given in Fig. A-14(b) and Fig. A-15(b). Based on this observation here, the AES analysis and the fractography seem to imply that the fracture path weaves inside the oxide layer (possibly closer to the oxide/graphite interface) then along the oxide/graphite interface or into the sub-surface layer of the graphite. The AES depth profile in Fig. A-16 furthermore, shows a thicker oxide film, about 16 - 20 nm at the interface region.

From all the observations and results discussed above, it seems reasonable to assume that the thickness of the oxide films sandwiched between aluminum and graphite has an important control on the interface bonding strength. When the oxide films are thin enough, the interface is more cohesive and bonded strongly with the graphite. There is obviously a limit to this since pure Al will not wet graphite at low temperature.[8] If the thickness of oxide increases beyond some critical value, the cohension of interface reduces significantly and becomes more susceptable to fracture. The critical thickness here ranged from approximately 8 to 16 or 20 nm.

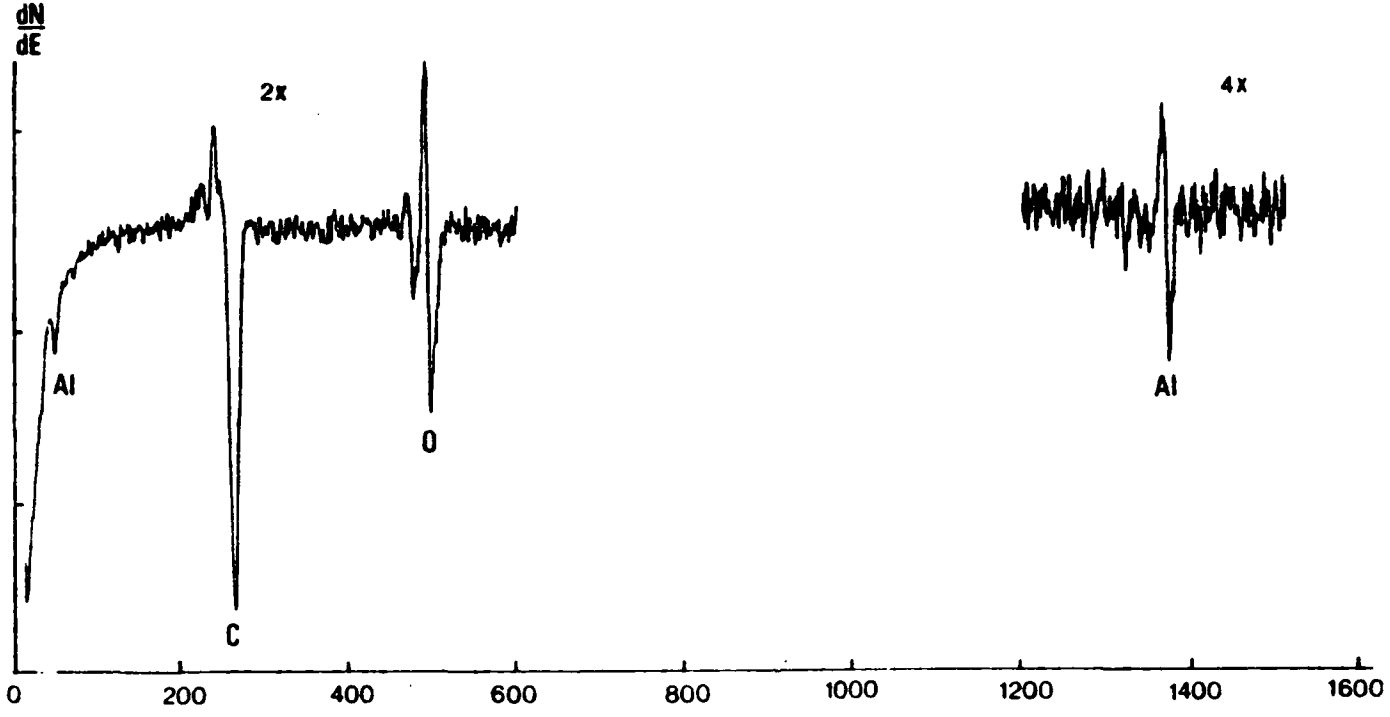

Fig. A-14. (a) AES spectrum of peeled area containing oxide for low vacuum samples.

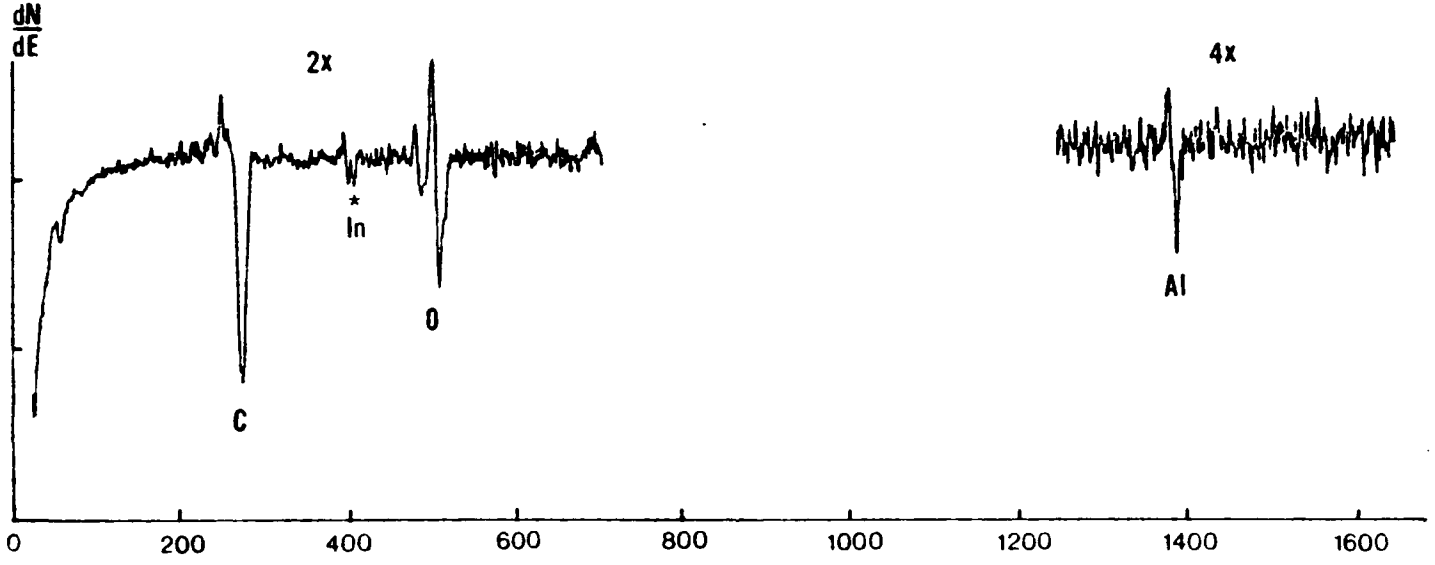

* Note: This indium peak is from chamber contamination.

Fig. A-14. (b) AES spectrum for an image scrap from the low vacuum sample.

Fig. A-15 (a). The SEM picture of fractography of peeled area showing some roughness and dimple.

Fig. A-15 (b) The SEM picture of an image scrap on the substrate. AES shown in Fig. 2-38(b).

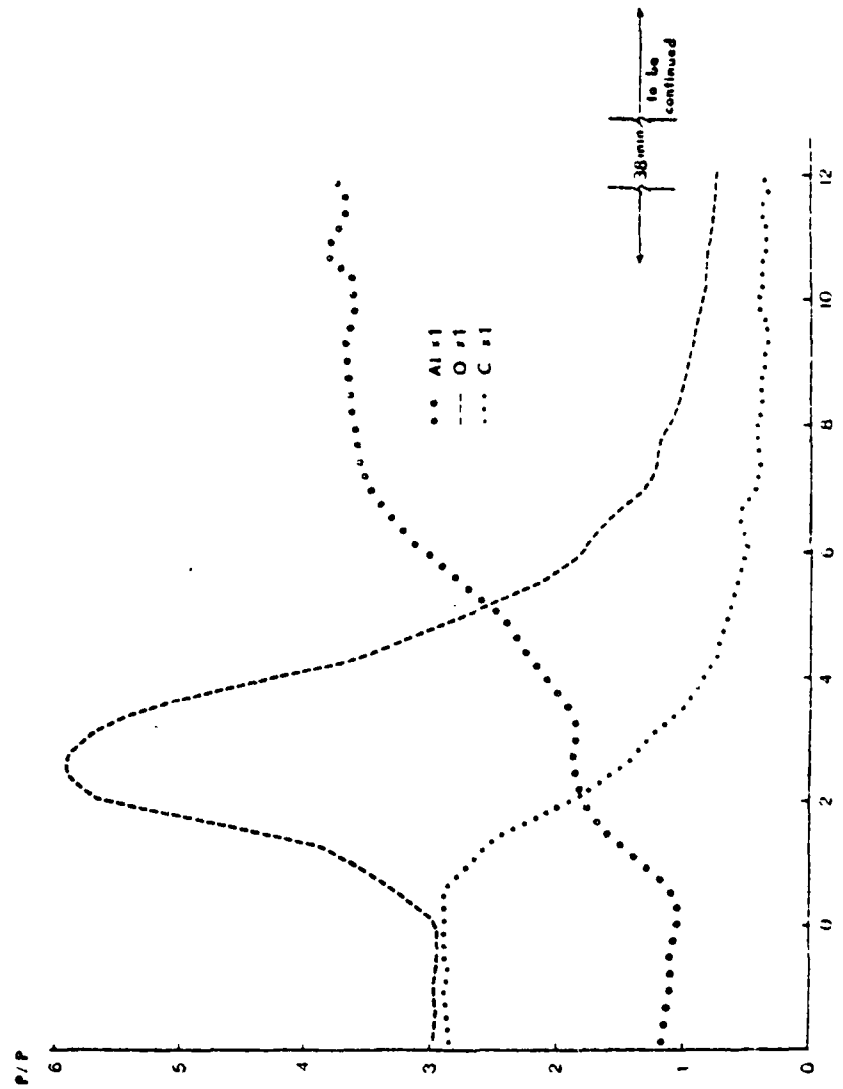

Fig. A-16. AES profile for low vacuum samples showing thicker oxide.

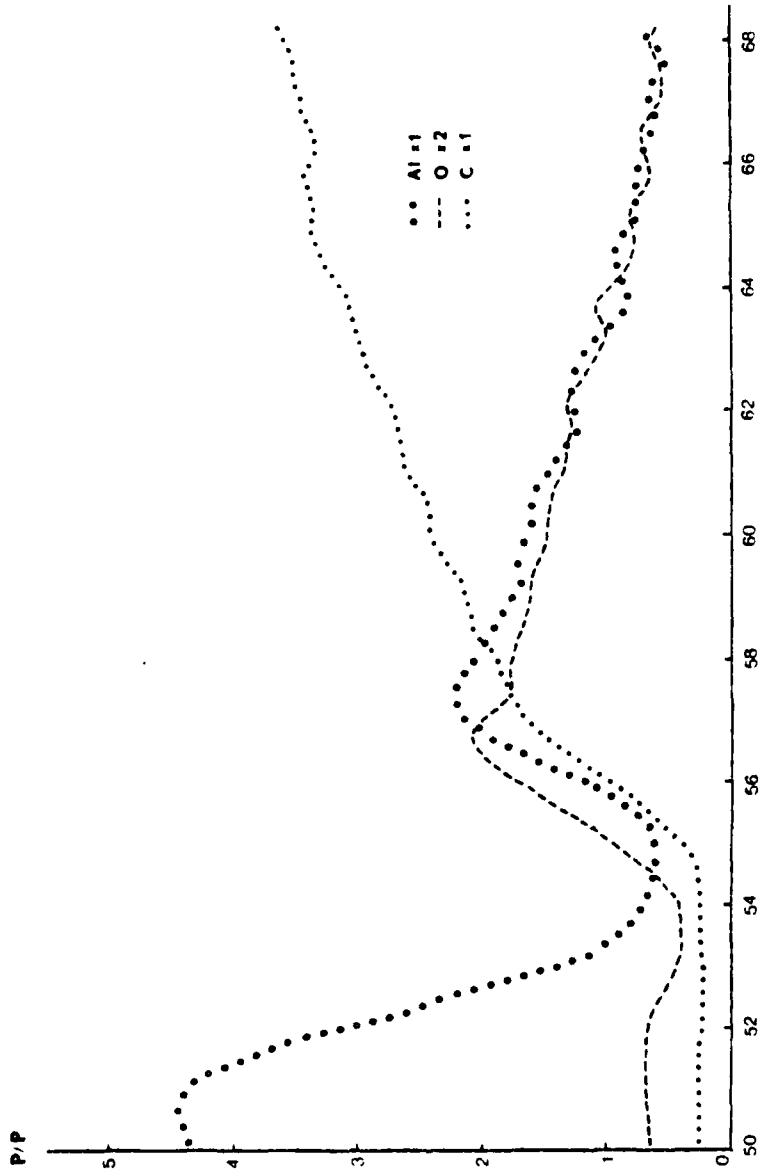
P/P
5
4
3
2
1
0
50
52
54
56
58
60
62
64
66
68
SPUTTERING TIME (min.)
Al =1
O =2
C =1

Fig. A-16. (con't.)

The electron primary beam energy for the AES spectra was 5KV, and the modulation energies were 3eV (for low energy part) or 6eV (for high energy part).

F. Discussion

The results presented indicate an influence of the interface oxide thickness on the weak path in the peel test. Thin oxides (~<10 nm) form a strong interface. Thicker oxides (~>10 nm) form a weak interface. A correlation is observed with the measured I-V curves.

One might also raise an interesting question: "Why do those junction systems which readily show low threshold and memory switching also exhibit the strong bonding in the interphase?" From a perspective model,[9] this is a reflection of the stability of disordered interphase bonding in the systems in which valence charge is more localized compared to delocalized charge available when the interphase begins to exhibit increasingly long range correlations. A situation that the long range order could happen is the appearance of crystalline phase. Thus, an interphase that readily re-organizes via electronic excitation from conductive (delocalized) to resistive (localized) states or vice versa could be near the limit of the mechanical instability.

References

1. W.N. Reynolds, "Physical Properties of Graphite," Elsevier Publishing Co., p. 5 (1968).

2. H.J. Stocker, Appl. Phys. Lett. 15, 55 (1969).

3. W. Doremus, Proc. Symp. on Semicond. Effect in Amorphous Solids, North Holland, Amsterdam (1970).

4. R.R. Verderber, J.G. Simmons, Phil. Mag. 16, 1049 (1969).

5. D.V. Morgan, M.J. Howes and R.D. Pollard, Thin Solid Film, 15, 123-131 (1973).

6. H.J. Hovel and J.J. Vrgell, J. of Applied Phys., Vol. 42, 12, 5076 (1971).

7. Private communication with Dr. R.M. Walser.

8. R. Sara, SAMPE 14, II-4A4 (1968).

9. Private communication with Dr. R.M. Walser for the Walser-Bene model.

Appendix B

X-Ray Analysis of Residual Stress Measurement in Aluminum-Graphite Composites

Due to the large difference in the coefficients of thermal expansion of the oriented graphite fibers and the aluminum matrix, a large residual stress pattern could be expected when the composite is cooled from the infiltration temperature to room temperature. This Appendix will first describe the x-ray techniques used to measure the residual stresses and then present and discuss the results obtained. The residual stress measurements were of the matrix phase. The results presented here were from the doctoral dissertation of Swe-Den Tsai.

1. Principles of Stress Measurement with X-Ray Diffraction

The fundamentals of determining the stress with X-ray diffraction have been derived in several sources. In this section, simple principles and methods related to the x-ray techniques applied here are presented.

Actually, the X-ray method is used to nondestructively measure the surface stress of the specimen. The depth of the defected region below the surface depends on the wavelength of the radiation. Fig. B-1 shows a space coordinate and the orientation of the stresses (or strains). Assuming the principle stress σ_1, σ_2 to lie in the surface,[1] the general surface stress, $\sigma\phi$, and corresponding strain are shown in Fig. B-1. The term ψ is the angle between the surface normal and the direction of strain being measured. According to the istropic continum elastic theory, the following relationship between principle stresses, surface stress and measured strain is given:[1]

$$\varepsilon\phi,\psi = \frac{1+\nu}{E}(\sigma_1\cos^2\phi+\sigma_2\sin^2\phi)\sin^2\psi - \frac{\nu}{E}(\sigma_1+\sigma_2) = \frac{d\phi\psi - do}{do} \qquad (1)$$

where E and ν are Young's modulus, and Poison's ratio respectfully. In this equation $d\phi,\psi$ is the lattice spacing at direction defined by ϕ,ψ and do is the interplanar spacing in the stress free state. The surface stress at angle ϕ is given by:

$$\sigma\phi = \sigma_1\cos^2\phi+\sigma_2\sin^2\phi \qquad (2)$$

and

$$-\frac{\nu}{E}(\sigma_1+\sigma_2) = \frac{d\phi,\psi=o-d}{do} \qquad (3)$$

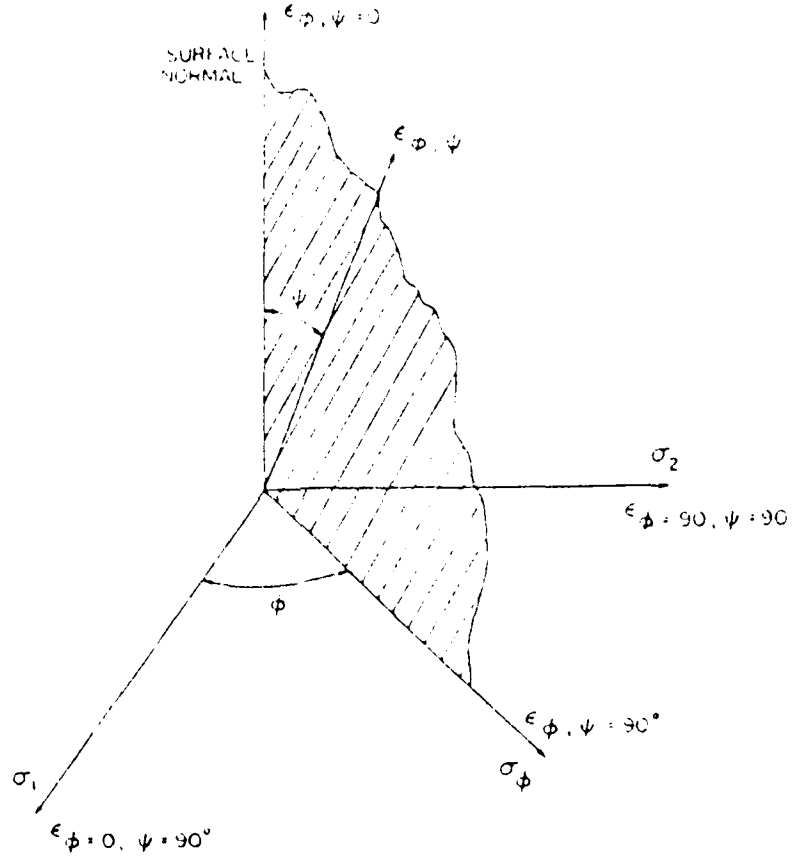

Fig. B-1 Definition of ϕ and ψ and Orientation of the stresses (or strains)

Substitute these equations into Eq. (1), we have

$$\frac{1+\nu}{E}\sigma\phi\sin^2\psi = \frac{d\phi,\psi - d\phi,\psi=o}{do} \qquad \frac{d\phi,\psi - d\phi,\psi=o}{d\phi,\psi=o} \tag{4}$$

Here, we approximate do with $d\phi\psi=o$ in the denominator. This replacement only leads to errors of 1-2 MPa, well within the tolerance in the measurement because even for the sample under very large stress the $d\phi\psi=o$ is not much different from do. This step eliminates the need to know the stress free d-spacing., and only the stressed specimen needs to be examined.

Experimentally speaking, this technique is determining the change in the interplanar spacing Δd, which will cause a corresponding change, $\Delta\theta$, in the Bragg angle of diffraction. Suppose the sample surface is in a tensile stress state. As the situation illustrated in Fig. B-2 (a), only certain grains are oriented to defract--those with planes of spacing d(hkl) parallel to the surface. Because of Poisson's effect, these planes could be in compression due to the residual tensile stresses. After the sample has been tilted, as in Fig. B-2 (b), different grains are diffracting; as these are oriented differently with respect to the stress than as shown in Fig. B-2 (a), the change in d-spacing and 2θ are different. It is these angular shifts due to the change in d-spacing that allows the strain due to a residual stress to be measured.

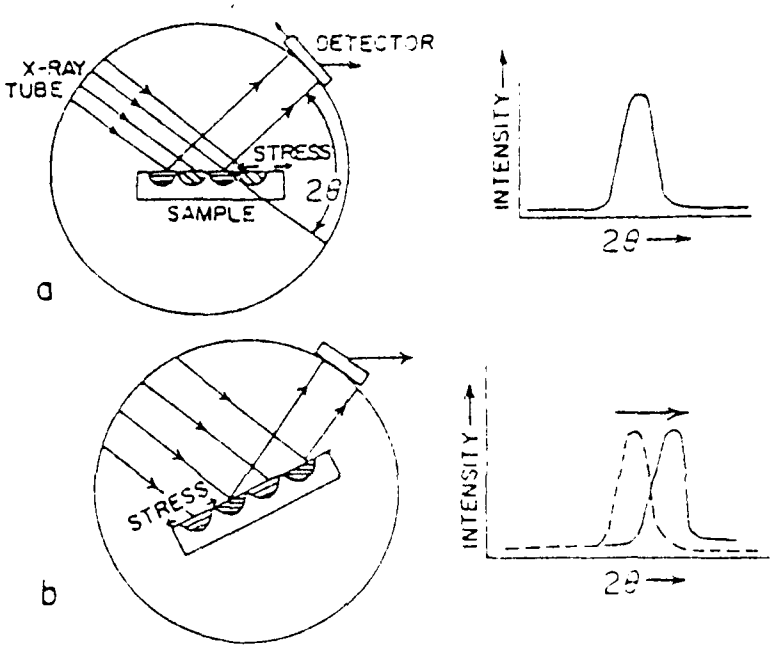

Fig. B-2. Schematic of a diffractometer for stress measurement.

(a) The atomic planes satisfy Bragg's law diffract X-Ray into a 2 θ value corresponding to a set of (hkl).

(b) After the specimen is tilted, diffraction occurs from other grains, but from the same set of planes. These are less close than in (a) due to the different poisson effects.

One thing to be noted is that equation (4) forms the basis of the analysis by relating a measurable change in the interplanar spacing $\varepsilon\phi,\psi$ to the surface stress. A stress will cause certain interplanar spacing of grains oriented at various angles to the surface to be different. Therefore, the interatomic spacing becomes the gage length. Variation of this gage length with orientation of the specimen, ψ, can be determined by several principle methods: the $\sin^2\psi$, two tilt and single exposure techniques. Only the $\sin^2\psi$ method was used here, therefore the description is limited to this method.

In the $\sin^2\psi$ method, several values of lattice strain are measured, each at a different tilt ψ of the specimen. It is then possible to determine the surface component of stress from a least-squares straight line fit for the lattice strain as a function of $\sin^2\psi$. The stress is then measured along the direction of the intersection of the ψ tilt and the specimen as illustrated in Fig. B-3.

Now, rewrite equation (4);

$$\frac{1+\nu}{E}\sigma\phi\sin^2\psi = \frac{d\phi,\psi - d\phi,\psi=0}{d\phi,\psi=0}$$

Now, let

$$\sigma\phi = \frac{m}{\left(\frac{1+\nu}{E}\right)} . \qquad (5a)$$

Here $m = \frac{\partial d\phi,\psi}{\sin^2}$. (5b)

In terms of interplanar spacing, it follows:

$$m^* = \frac{\partial d\phi,\psi}{\partial \sin^2\psi} \quad , \tag{6a}$$

then: $$\phi = \frac{m^*}{d\phi,\psi=o(\frac{1+\nu}{E})} \tag{6b}$$

Four to six ψ tilts are normally employed to determine the interplanar spacing as function of ψ.

2. Experimental and Analytical Procedures

The residual stresses of Graphite-Aluminum composites were measured utilizing the diffractometer technique to quantitatively record the intensity profiles. Two kinds of diffractometers with different geometrical configuration and optics were applied: the classical Bragg-Brentano diffractometer, also called ω-diffractometer, and ψ-diffractometer, which is similar to the Schulz method for pole figure determination. The classical ω-diffractometer was the most common instrumental arrangement for many years. While still in heavy use in the United States, it is being superceded by the "ψ-diffractometer" in Europe and Japan.

2-a. ω-Diffractometer

In the ω-diffractometer, the ψ tilt angle is obtained by rotating the specimen on the goniometer axis independently of

the counter, or say, parallel to the 2θ axis. As seen in Fig. B-3, this would produce a new focal point. In order to achieve the best possible focusing during the ψ inclination, the receiving slit and the detector must be moved to a new point C in Fig. B-3 (b). The motion of the receiving slit must be truly radial or an error will occur. This distance of moving could be determined according to:[1]

$$R_p = R_G \frac{\cos(\psi+(90°-\theta))}{\cos(\psi-(90°+\theta))}$$

where R_p represents the distance from the sample at focus position, and R_G is the goniometer radius.

Because of the optics used, an ω-diffractometer is also referred to as a parafocusing diffractometer. This optical arrangement is inherently sensitive to sample displacement. If the sample is displaced from the center of the diffraction circle, there is a relative shift of diffracted rays between different tilt ψ=0 and $\psi=\psi_o$, as in Fig. B-4. Therefore the sample displacement, Δx, could be determined through Neilson-Riley lattice parameter extrapolation,[2] then eliminated by moving the sample toward or away from the center.

2.b. ψ-Diffractometer

The stress measurements were also made on a "ψ-diffractometer," where the specimen is rotated around an axis lying parallel to the diffractometer plane, i.e., normal to the goniometer axis, as in Fig. B-5. The principle characteristics and application have been summarized by Macherauch and Wolfstieg.[3] This diffractometer,

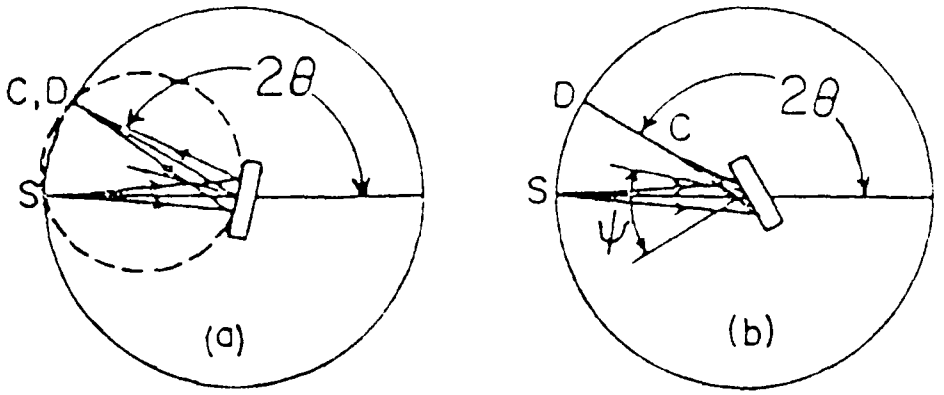

Fig. B-3. ω-diffractometer. The ψ angle is tilted around the axis perpendicular to the drawing.

(a) specimen is on the focusing circle when ψ=0.

(b) the focus moves when the specimen is tilted ψ.

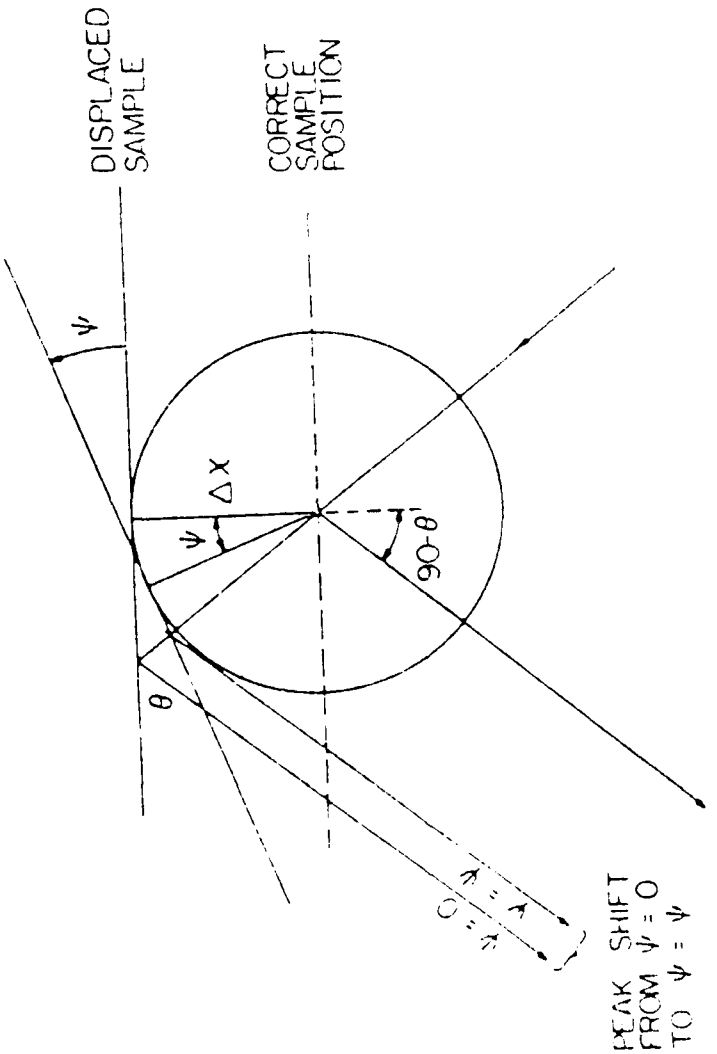

Fig. B-4. Effect of sample displacement Δx on the peak position after the sample is tilted.

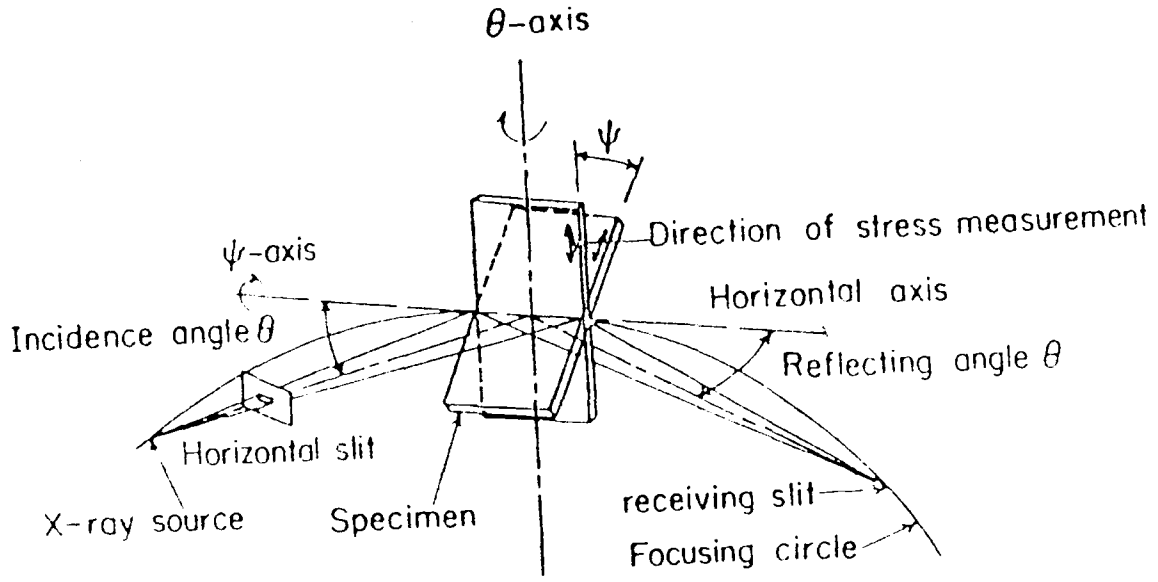

Fig. B-5. ψ-diffractometer. The ψ angle is tilted around a axis in the plane defined by the incident and diffracted beams.

often referred to as the "side-inclining procedure" has its unique advantages lying in the fact that the incident and diffracted rays are equal path lengths and independent of ϑ,ψ and vertical divergence. During rotation of the specimen around the ψ axis, the X-ray tube, specimen surface and the counter all remain on the focusing circle eliminating the relocation of the receiving slit to obtain optiman focusing. As the path length for incident and scattered beams inside the specimen is the same, we don't need the absorption correction after a ψ-tilt as we do for the ω-diffractometer.

Except for many of the unpredictable sources of error which depend on either alignment, sample position or electronic stability, there are some predictable factors influencing the bias in the precision control: The following will be concerned with their effects and significancy to our experiment:

(a) Lorentz-Polarization factor

This term combines two 2θ dependent intensity corrections, the Lorentz factor and Polarization factor which are important in both ω and ψ diffractometer. The conventional correction factor for filtered radiation designeted L_p, is:[4]

$$L_p = \frac{1+\cos^2 2\theta}{\sin^2\theta}$$

(b) Absorption factor

This is significant in ω-diffractometer. For a flat sample the measured intensity is corrected by dividing by:[5]

$$ABS = 1 - \tan\psi \cot\theta$$

(c) Atomic scattering factor and temperature factor

For alloys these two terms are often complex and usually neglected. The Debye temperature factor is a very small correction relative to the others. Since we are measuring the stress of aluminum matrix in composite, the atomic scattering factor for aluminum metal was incorporated in the correction. The temperature factor was not considered.

After the intensity distributions have been corrected by these factors, the angle of the diffraction peak for various ψ tilts could be determined from a consistent feature of line profile. Since in residual stress measurement using X-ray diffraction, the profile has been traditionally defined in U.S. by the apex of a parabola fit to the top region of intensity curve. The data points were selected following the rule of using only approximately the top 15%, then fitting the points to a parabola by least squares fit.

Eleven data points were selected to accumulate the counts instead of regular three or five points parabola for both type of diffractometers. The use of these multiple data points (rather than three) and a least-squares parabolic fit have been demonstrated to improve the reproducibility significantly in a computer automated data collection system.[6] The eleven data point profile is not necessary for manual collection system. The reason for using the eleven point parabolas were used in both types of diffractometers was to keep the analysis consistent.

The ω-diffractometer measurements were made at Northwestern University on a computer controlled Picker-diffractometer following the parafocusing geometry. The hardware, software and its capability were described elsewhere.[6] $Sin^2\psi$ angle tilts taken in equal increments were employed. In order to counteract grain size effect, 2θ-oscillations of 2 degrees were employed when necessary. The matrix grain size here is approximately a few tenths of a millimeter. The cobalt X-ray source of 0.15 cm^2 apeture size was employed. About 90 percent of intensity came from a depth of 5.4×10^{-3} cm of sample surface. Because of the ease of doing, repetitive peak determination and the method of collecting counts on the selected data points in this automated system, only the data with a correlation factor of 0.95 or above in the linear least-squares fit for d versus sin^2 were considered reliable. For the ψ diffractometer, a Siemens texture diffractometer with adjustable beam size apeture was applied, and the GE X-ray source combined with this Siemens diffractometer was also used for some of the specimens. The manual step scans of 2θ for the data accumulation were controlled carefully. Although this required a tedious and time consuming procedure, there was flexibility in choosing peak position and breadth which varies with sample, residual stress level and ψ angle which are limited in the automatically controlled diffractometer. Furthermore, the remarkable advantages in optics and geometry for the ψ-tilt described earlier in this section made this technique superior. A copper radiation source was used. A horizontal beam size of 0.1×0.5 cm^2 was adjusted

in the beam aperture. The raw data were then processed by a computer program. The peak locations and the stresses were thus determined. Either fix-count or fix time accumulation procedures were used to maintain good statistical errors. The plots of various peak apex regions analyzed and the $d\psi$ versus $\sin^2\psi$ could be obtained through the choice of different versions in computer programs. Those alternative versions of computer program and binary codes are saved in a permanent file.

The residual stress measurements were made on many of the Graphite-Aluminum Composites described earlier. Different fiber type and processing methods were used to produce the composites studied here. The variation of fiber properties and processing procedures could modify the mechanical properties as well as the stress state on the interface area. The characteristics of component with corresponding composite are listed in Table B-1. All the materials here, except the Pitch/6061 G4371 and G4411, were produced using the standard Ti-B CVD coating process onto the graphite fibers prior to passing the fiber tow through the aluminum melt. Pyrolytic carbon coating prior to the Ti-B processing was used in G3437 and precoating of porcelain enamel[7] was applied in PANII/6061 G3675. The Pitch/6061 G4731 had a layer of SiO_2 on the fiber surface using an orgametallic solution coating technique. The precursor wire produced by these processing methods were then consolidated into

Table B-1

Components and Properties

Composites	Fiber	Base	Young's Modulus of Fiber $x10^6$ psi	Matrix
G3394	Thornel 50	Rayon	60	Al 201
G3437	Thonel 300	PAN II	34	Al 201
G3675	Celion 6000	PAN II	35	Al 6061
G3669	Celion 6000	PAN II	35	Al 6061
G4371	VSB-32	Pitch	55	Al 6061
G4411	VSB-32	Pitch	55	Al 6061

* The matrix of G3394 and G3437 are Al 201. Matrix for the other composites are Al 6061. Young's modulus for Al 201 and 6061 are 10.2 and 10 (Mpsi). The yield strength are 35 Ksi and 37 ksi respectively.

plate form by diffusion bonding. Residual stress measurements were also made on the samples of Rayon/201 G3394 and PANII/201 G3437 quenched to liquid N_2 temperature and then tested at room temperature. To establish base line data composite Rayon/201 G3394 with high modulus fiber and the low modulus fiber composite G3437 which has about one half transverse strength of G3394 were selected to see the effects of the thermal expansion mismatches and correlation with transverse strength. The PANII/6061 G3675 and G3669 were chosen because of the high contents of Al_4C_3. The G3675 is a extreme case of very high tranverse strength with a degraded longitudinal strength. The composite G3471 and G4411 with high modulus fiber VSB-32 and 6061 Al alloy matrix were also analyzed here. The measurements of the liquid nitrogen quenched samples were to change the residual stress patterns and to relate them to the transverse strengths measured before and after quenching.

Due to the relative large divergent beam impinging on the sample surface and the penetration depth greater than a monolayer of fibers, the stress measurement obtained was a volume average over the matrix, similar to the one represented by the dotted line in Fig. B-6. For such a volume average, the penetration depth of X-ray becomes an important parameter. Since it is the stress in the vicinity of the interface that is of interest here, it is essential to expose the interface in the specimen to the X-rays.

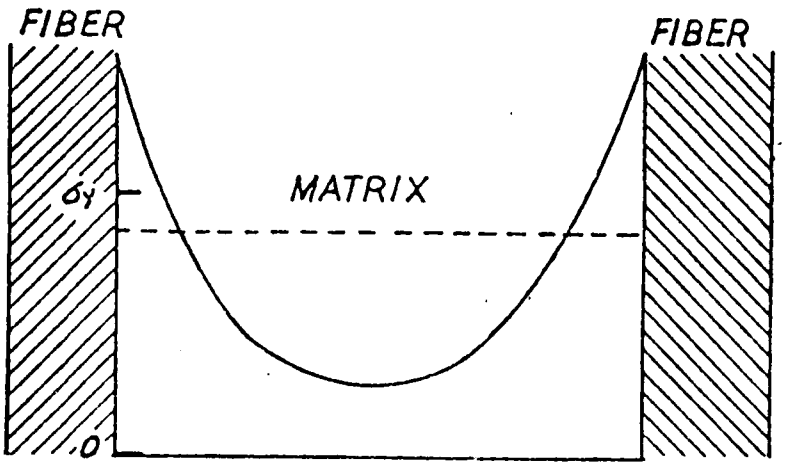

Fig. B-6. A simple model to show the residual stress distribution. The dotted line is an average value. The term σ_y is the yield strength of the matrix.

In other words, the penetration depth should be such that the X-rays average over the region which includes interfaces.

In the preparation of the samples, mechanical polishing was not used, since it could introduce extra residual stress. By electropolishing, enough surface material could be removed so as to expose the interface area, and to get rid of the surface layer that may have been stressed by mechanical work. The electrolyte used here was a solution of one part concentrated nitric acid in 3 parts of methanol by volume. The currents in the electro-polishing circuit were dependent on the area of the samples to be polished, and polishing time was kept consistently or varied for the different thickness to be removed. For Rayon/201 G3394, PANII/6061 G3437, and G3669, Pitch/6061 G4371 and G4411 the sample surfaces were polished just enough to expose portions of interfaces. With PANII/6061 G3675, a sample with light electrolytic polishing was prepared. This resulted in a thin surface layer of aluminum above the fibers having thickness greater than the penetration depth of the X-rays. Thus, during volume averaging only the aluminum matrix containing no fibers would be covered. In addition, a heavier polishing was also done on the sample of Pitch/6061 G4411 composite to reach the deeper region down into the surface, after the stresses of the normally polished surface were measured. The stress levels then could be compared versus the distance from the surface of the sample. Specimens used were plates with the approximate thickness from 0.15 to 0.4 cm, and dimensions 1.9 to 2.5 for the

width and length. The area of plates was large enough so that the beam divergence could stay within the center portion of the specimens. Residual stress measurements were made in both the longitudinal and transverse directions to the fiber axis, as indicated in Fig. B-7.

3. Result and Discussion

The high angle peak of aluminum (420) diffraction was used for the stress measurements to achieve high accuracy. The residual stress determined using ω-diffractometer system are listed in Table B-2 and those measured by ψ-diffractometer arrangement are listed in Table B-3. The tables also list the transverse and longitudinal strengths of composites and the correlation factors for the least squares straight line fit for the lattice strain VS $\sin^2\psi$.

It may be noted that the longitudinal direction stress values for Rayon/201 G3394 and PANII/201 G3437 are comparable to the nominal 240 Mpa yield strength of the 201 Aluminum matrix. This can be explained by the mismatch of thermal expansion coefficients between two components. Table B-4 presents this difference in thermal properties. In the graphite fiber/aluminum composite Rayon/201 G3394, there is a mismatch of approximately $23 \times 10^{-6}/^{\circ}C$ in the thermal expansion coefficients along the longitudinal direction. The sample is cooled by almost 600 C after solidification, giving rise to significant amounts of residual stresses in the fiber direction. A calculation using a planar model[9] and a cylinder model with proper boundary conditions[10] show that stresses

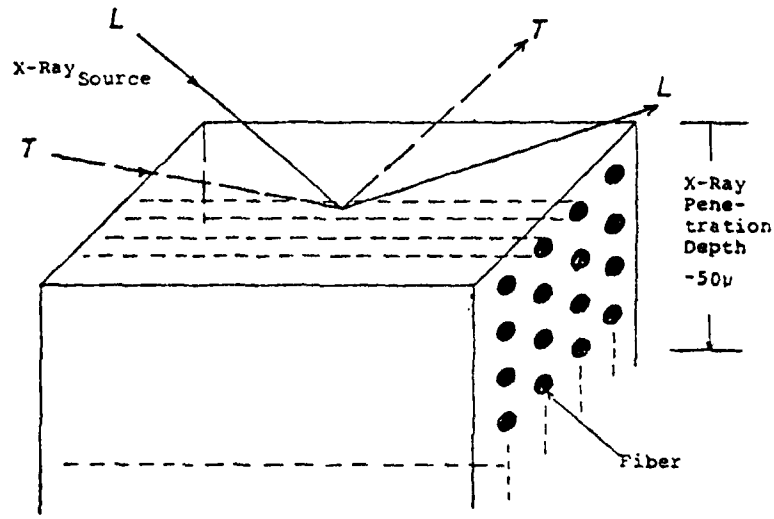

Fig. B-7. Stress measurement geometry.

L - Longitudinal

T - Transverse

Table B-2

Residual Stresses Measured from θ-diffractometer

Material	Transverse Strength MPa	Longitudinal Strength	Direction of Measurement	Residual Stress MPa	Correlation Coefficient
G3437	10	1120	L	199.38	0.9640
			T	166.28	0.9658
G3394	20	763	L	228.38	0.9945
G3675 (lighter polishing)	75	259	L	40.71	0.9507
			T	33.26	0.9788
G3437 (cooled to liq. N_2 temp. & measured at room temperature)	10 (before quench)	1120	L	144.11	0.9856
			T	120.20	0.9924

L = Longitudinal direction

T = Transverse direction

Table B-3

Residual Stresses Measured from ψ-diffractometer

Material	Transverse Strength MPa	Longitudinal Strength	Direction of Measurement	Residual Stress MPa	Correlation Coefficient
G3394	20	763	L	213.75	0.987
			T	72.40	0.875
G3675 (No. 1)	75	259	L	42.06	0.971
			T	40.33	0.988
G3675 (No. 2)			L	46.38	0.986
			T	26.44	0.970
G3669	28	303	L	68.03	0.956
			T	39.54	0.969
G4371	10	892	L	58.52	0.991
			T	60.44	0.988
G4411	7	565	L	55.48	0.999
			T	56.83	0.914
G4411 (heavier polishing)			L	55.48	0.999
			T	82.68	0.885
G3394 (quenched to liq.N_2 temp and measured at room temperature)			L	131.94	0.900
			T	-46.00	0.983

Table B-4

Thermal Expansion Coefficient of Component Materials

Components	Thermal Expansion Coefficient $10^{-6}/°C$
Thornel 50 (Fibers in G3394)	$-0.1 \sim -0.54\alpha_{fL}$ (Axial direction) to about 300°C
	25 (Transverse direction)
Thornel 300 (Fibers in G3437)	$8.0^{*}\alpha_{fT}$
	$-0.7^{*}\alpha_{fL}$
Al-201 Matrix of G3394, G3437	23.22
Celion 6000	assumed the same as Thornel 300
Al-6061 Matrix of G3675, G3669, G4371, G4411	23.58

* The values here were taken from Reference 8.

well above the yield strength of aluminum exist at the interface of the aluminum matrix-graphite fiber. Plastic flow could be expected to occur because of the high values of thermally-induced stresses. Assuming no debonding, a stress gradient is expected in the Al matrix, with above-the-yield strength stress at the interface. A schematic of the expected stress distribution is given in Fig. B-6. The dotted line represents the measured average value of stress in the aluminum matrix. All of the matrix is expected to be in a state of tensile stress minimized at a point between fibers.

While there is a significant difference in thermal expansion coefficients of Al and graphite in the longitudinal direction, this difference is negligible in the transverse direction for Rayon/201 G3394 due to the anisotropy of the graphite fiber. Hence, the thermally-induced residual stresses in the transverse direction are not expected to be as high as those in the longitudinal direction. These transverse residual stresses are mechanical in origin, since a tensile residual stress state[11] is introduced in the matrix after cooling the composite from elevated temperatures.[12]

In composite PANII/201 G3437, the residual stresses are large and very close to those measured in Rayon/201 G3394 in the longitudinal direction. This could be expected, since the mismatch of thermal expansion coefficients along the fiber direction in PANII/201 G3437 is similar to that in Rayon/201 G3394. As for the

residual stresses in the transverse direction, PANII/201 G3437 has the stress level a little higher than those in Rayon/201 G3394; they have values of 116 Mpa and 73 Mpa respectively (see Table B-2 and Table B-3). This situation is due to the moderately large thermal expansion coefficient mismatch, a value of about $15 \times 10^{-6}/^{o}C$ (see Table B-3).

The lower levels of stresses, however, were observed in the composites PANII/6061 G3675 and G3669 which are fabricated from a PAN II base Celion 6000 fibers with 6061 aluminum matrix. The nominal physical properties of this fiber should be very much close to those in the Thonel 300 fibers of the same PAN II base material. The thermal expansion could be expected to increase or decrease as the fiber modulus decrease or increase in the longitudinal axial direction since both properties are closely related to the degree of crystal prefered orientation (see Table B-1 and B-3). Presumably, the mismatches between fiber and matrix could be expected as the same as in the case of PANII/201 G3437, therefore, the similar stress levels should be measured. However, the low modulus PAN II fibers are highly reaction with molten Aluminum during the infiltration process and aluminum carbide, Al_4C_3 is easily formed in the interface region. This high activity is closely related to the surface characteristics of the fiber, i.e. preferred orientation in graphite crystallites. Generally speaking, the highly graphitized high modulus fibers are less reactive with Al in the infiltration process while the low modulus fibers are badly degraded.

In PANII/6061 G3675 and G3669, the Al_4C_3 content is higher than the average amount, while the content in PANII/201 G3437 is much lower than the average one. This reduction in Al_4C_3 results from the application of the oriented pyrolitic carbon layer, which limits fiber-matrix interaction. A comparison of the Al_4C_3 contents in those composite systems is given in Table B-5.[13] The formation of a large amount of carbide layer at interface effectively provides a "grading seal" that can relieve the residual stress pattern in the interphase region. This is due to a thermal expansion coefficient of Al_4C_3 is about $10x10^{-6}/°C$ as estimated from the melting temperature (2750°C) relationship with thermal expansion.[14] This value is halfway between those for aluminum and the graphite fiber. Consequently, the residual stress levels are reduced to a relatively low value. Actually, the model described in Fig. B-6 did not consider a finite thickness interphases. It has been observed in the TEM study that oxides, carbides, and/or borides are present at the fiber-matrix interface. Since the mismatch between the thermal coefficients of the compounds and the aluminum matrix are lower than that of fiber and aluminum in the longitudinal direction, the maximum longitudinal residual stress at the interfaces can be expected to be lower than when a simple graphite-aluminum interface exists.

Relative low stresses also were measured in the VSB-32 pitch/6061 aluminum composites, G4371 and G4411. There was little in the residual stresses between those before heavier electrolytic

Table B-5

Al_4C_3 Contents in Composites

Composites	Al_4C_3 Content ppm
G3437 PANII/201 (Pyrolitic carbon coated)	690
G3675 PANII/6061	3644
G3669 PANII/6061	9387

polishing and after. The heavier polishing removed 100~120μm thickness from the normally polished surface. Because of the high modulus and thus the highly preferred orientation of basal plane along the fiber axis, a low axial thermal expansion coefficient α_{fL} close to the value in T 50 fiber is expected. Correspondingly, a large expansion mismatch should exist in the longitudinal direction of the fiber. Assuming the good bond was formed at interfaces, the lower residual stresses observed could be attributed to the relaxation effect of the thin composite plate used, since only two or three plies of precursor wires were consolidated to make these plates. This can be compared to the four to six layers with aluminum wrapping for the other plates. The thicknesses are about 0.15 cm and approximately 1/3~1/2 of those in the other materials. Then, the stresses may not be fully constrained in the composite plates.

When the high residual stress samples Rayon/201 G3394 and PANII/201 G3437 composites were quenched in liquid nitrogen and annealed at room temperature, approximately 30% reduction in residual stress was observed. The cryogenic cooling induces additional plastic flow in the matrix, establishing a new elastic condition at the cryogenic temperature. Heating the composite back to room temperature will then relieve much of the residual stresses. However, the 30% is less of a reduction than is expected. Additional work hardening at the interface occurring during cooling may explain this difference between the measured and calculated changes.

A recent study of the cryogenic cooling effect on the transverse strengths in some materials used here indicated that the transverse strength of composite did not change significantly before and after quenched in liquid nitrogen.

A sample of Rayon/201 G3394 composite was used as a standard and the measurements were made in both ω and ψ diffractometer. The very good agreement found assured that the measurements from both types of diffractometer are consistent and comparable.

4. Summary

Thus, x-ray diffraction can be very effectively applied to determine average residual stresses due to the mismatch in thermal expansion coefficients in the graphite-aluminum composite system. The indications are that the residual stresses averaged through the distribution in aluminum matrix are not directly related to the transverse strengths. The basic properties related to the interface strength are associated with the multiple interfaces between the various phases such as oxide, carbide, boride layers and the complexity of the metallurgical interactions. However, the x-ray residual stress measurement described in this Appendix helps in the understanding of how the components and their properties influence the interfacial behavior.

References

1. M.E. Hilley, J.A. Larson, C.F. Jatczak and R.E. Ricklefs, "Residual Stress Measurement by X-Ray Diffraction," SAE Information Report, J. 784a, SAE Pennsylvania (1971).

2. J.B. Cohen, "Report on Tungsten Lattice Parameter Round Robin," X-Ray Subcommittee of SAE Iron and Steel Technical Committee, Division 4 (Nov. 1964).

3. F. Macherauch and U. Wolfstieg, Adv. in X-Ray Analysis, 20, 369-377 (1977).

4. J.B. Cohen, "Diffraction Methods in Materials Science," MacMillan Co., New York, p. 225 (1966).

5. D.P. Koistinen and R.E. Marburger, Trans. ASM. 51, 537-555 (1959).

6. M.R. James and J.B. Cohen, Adv. in X-Ray Analysis, 20, 291-308 (1977).

7. G.L. Steckel, R.H. Flowers, and M.F. Amateau, "Transverse Strength Properties of Graphite-Aluminum Composites," in Failure Modes in Composites IV, J.A. Cornie and F.W. Crossman, eds. Conference Proceedings, The Metallurgical Society of AIME (Fall 1977).

8. T. Ishikawa and S. Kobayashi, Thermal Expansion Coefficients of Unidirectional Fiber-Reinforced Composites, part 1 and 2, J. Jpn. Soc. Aeronaut. Space Sci., Vol. 25, pp. 394-400, 423-429 (1977).

9. C.A. Hoffman, "Effects of Thermal Loading on Composites with Constituents of Differing Thermal Expansion Coefficients," NASA-TN-D 5926 (1970).

10. S.S. Hecker, C.H. Hamilton and L.J. Ebert, "Elastoplastic Analysis of Residual Stresses and Axial Loading in Composite Cylinders," Journal of Materials, JMLSA, Vol. 5, No. 4, pp. 868-900 (Dec. 1970).

11. J. Gayda and L.J. Ebert, Met. Trans., 10A, 349-353 (1979).

12. Masuji Vermura, Hisashi Iyama and Yoshiko Yamaguchi, J. of Thermal Stresses, 2, 393 (1979).

13. F. Padlla, W.C. Harrigan, Jr. and M.F. Amateau, "Handbook of Test Methods for Evaluation and Qualification of Aluminum-Graphite Composite Materials," Materials Sciences Laboratory, The Aerospace Corporation, El Segundo, CA (21 Feb. 1975).

14. C. Zwikker, "Physical Properties of Solid Materials," London, Pergamon Press (1954).

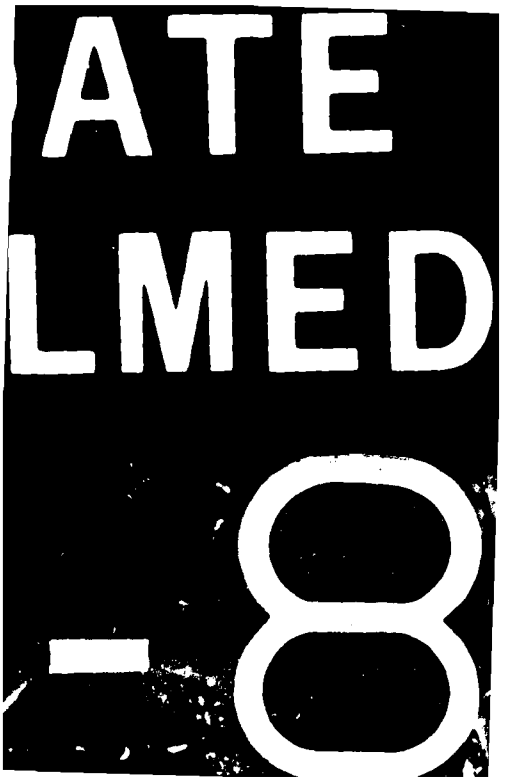
ATE
LMED
-8